

Electronic Structure of the Water Oxidation Catalyst $cis,cis-[(bpy)_2(H_2O)Ru^{III}ORu^{III}(OH_2)(bpy)_2]^{4+}$, The Blue Dimer

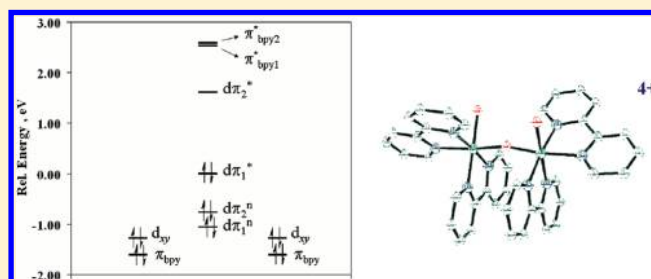
Jonah W. Jurss,[†] Javier J. Concepcion,[†] Jennifer M. Butler,[‡] Kristin M. Omberg,[‡] Luis M. Baraldo,[‡] Darla Graff Thompson,[‡] Estelle L. Lebeau,[‡] Brooks Hornstein,[‡] Jon R. Schoonover,[‡] Hershel Jude,[§] Joe D. Thompson,[§] Dana M. Dattelbaum,[⊥] Reginaldo C. Rocha,[§] Joseph L. Templeton,[†] and Thomas J. Meyer^{*,†}

[†]Department of Chemistry, University of North Carolina, Chapel Hill, North Carolina 27599-3290, United States

[‡]Materials Science and Technology Division, [§]Materials Physics & Applications Division, and [⊥]Dynamic & Energetic Materials Division, Los Alamos National Laboratory, Los Alamos, New Mexico 87545, United States

S Supporting Information

ABSTRACT: The first designed molecular catalyst for water oxidation is the “blue dimer”, $cis,cis-[(bpy)_2(H_2O)Ru^{III}ORu^{III}(OH_2)(bpy)_2]^{4+}$. Although there is experimental evidence for extensive electronic coupling across the μ -oxo bridge, results of earlier DFT and CASSCF calculations provide a model with magnetic interactions of weak to moderately coupled Ru^{III} ions across the μ -oxo bridge. We present the results of a comprehensive experimental investigation, combined with DFT calculations. The experiments demonstrate both that there is strong electronic coupling in the blue dimer and that its effects are profound. Experimental evidence has been obtained from molecular structures and key bond distances by XRD, electrochemically measured comproportionation constants for mixed-valence equilibria, temperature-dependent magnetism, chemical properties (solvent exchange, redox potentials, and pK_a values), XPS binding energies, analysis of excitation-dependent resonance Raman profiles, and DFT analysis of electronic absorption spectra. The spectrum can be assigned based on a singlet ground state with specific hydrogen-bonding interactions with solvent molecules included. The results are in good agreement with available experimental data. The DFT analysis provides assignments for characteristic absorption bands in the near-IR and visible regions. Bridge-based $d\pi \rightarrow d\pi^*$ and interconfiguration transitions at Ru^{III} appear in the near-IR and MLCT and LMCT transitions in the visible. Reasonable values are also provided by DFT analysis for experimentally observed bond distances and redox potentials. The observed temperature-dependent magnetism of the blue dimer is consistent with a delocalized, diamagnetic singlet state ($d\pi_1^*$)² with a low-lying, paramagnetic triplet state ($d\pi_1^*$)($d\pi_2^*$)¹. Systematic structural–magnetic–IR correlations are observed between $\nu_{sym}(RuORu)$ and $\nu_{asym}(RuORu)$ vibrational energies and magnetic properties in a series of ruthenium-based, μ -oxo-bridged complexes. Consistent with the DFT electronic structure model, bending along the $Ru-O-Ru$ axis arises from a Jahn–Teller distortion with $\angle Ru-O-Ru$ dictated by the distortion and electron–electron repulsion.



INTRODUCTION

The blue ruthenium dimer, $cis,cis-[(bpy)_2(H_2O)Ru^{III}ORu^{III}(OH_2)(bpy)_2]^{4+}$ ($bpy = \text{bipyridine}$), was first reported as a water oxidation catalyst in 1982.^{1,2} It is oxidatively activated by proton-coupled electron transfer (PCET) through a sequence of $1e^-$ intermediates to give the reactive transient $[(bpy)_2(O)Ru^VORu^V(O)(bpy)_2]^{4+}$. The latter undergoes rapid O-atom transfer to water to give a peroxidic intermediate, which is further oxidized, resulting in oxygen release before reentering the catalytic cycle.^{3–6}

The electronic structure properties of the blue dimer, obviously of interest in understanding this molecule and how it functions as a catalyst, have been a source of controversy. The purpose of this paper is to summarize the properties of the blue dimer and emphasize the role of strong electronic coupling

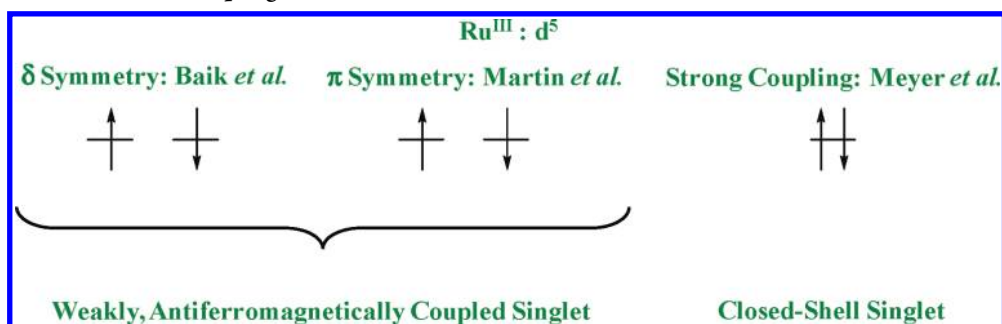
between the nominally Ru^{III} ions across the μ -oxo bridge. For example, compared to structurally related monomers, electronic coupling provides access to the higher oxidation state “ Ru^V ” at relatively low potentials and is a key to facile water oxidation.^{2–4,6–10} By now, a number of single-site water oxidation catalysts have been identified and their mechanisms elucidated by kinetic, spectroscopic, and theoretical analysis.¹⁰ The results of these studies highlight the importance of higher-oxidation-state oxo forms, O–O bond formation, and peroxide intermediates.¹⁰

Earlier density functional theory (DFT) calculations predicted a ground-state triplet for the blue dimer with

Received: July 18, 2011

Published: January 24, 2012

Scheme 1. Proposed Electronic Coupling Schemes for the Blue Dimer



relatively weak electronic coupling and Ru^{III} magnetic exchange across the μ -oxo bridge. On the basis of the results of DFT (B3LYP) and complete active space self-consistent-field (CASSCF) calculations,¹¹ Batista and Martin concluded that the ground state is a weakly antiferromagnetically coupled singlet state with partial electronic delocalization by $d\pi$ – $d\pi$ mixing across the μ -oxo bridge. In contrast, Yang and Baik invoked antiferromagnetic coupling by $d\delta$ – $d\delta$ mixing across the bridge (Scheme 1).¹²

The molecular structures for both *cis,cis*-[(bpy)₂(H₂O)-Ru^{III}ORu^{III}(OH₂)(bpy)₂]⁴⁺ and *cis,cis*-[(bpy)₂(HO)-Ru^{IV}ORu^{III}(OH₂)(bpy)₂]⁴⁺ have been determined crystallographically, and structural information is available for a number of derivatives.^{2,8,14,15} Electronic and molecular structures in the blue dimer¹¹ and its higher oxidation states,^{12,16} and possible mechanisms of water oxidation, have been investigated by DFT.^{12,13}

We report here the results of an extensive series of experiments and results of DFT calculations that explore, in detail, the electronic and molecular structures of the blue dimer. These results demonstrate that strong electronic coupling exists and has a profound influence on the molecular and electronic properties.

EXPERIMENTAL SECTION

Materials. High-purity water was further purified by a Millipore system. $\text{RuCl}_3 \cdot 3\text{H}_2\text{O}$ was purchased from Pressure Chemicals. All other reagents were purchased from Sigma Aldrich and used as received, including Na_2SO_4 , which was utilized as an internal standard in resonance Raman experiments.

Preparation of Complexes. The salts [(bpy)₂(H₂O)-Ru^{III}ORu^{III}(OH₂)(bpy)₂](ClO₄)₄ and [(bpy)₂(H₂O)-Ru^{III}ORu^{IV}(OH)(bpy)₂](ClO₄)₄ were synthesized as previously described.² The hexafluorophosphate salt, i.e., [(bpy)₂(H₂O)-Ru^{III}ORu^{III}(OH₂)(bpy)₂](PF₆)₄, was synthesized in an analogous fashion but isolated by the addition of excess NH_4PF_6 to an aqueous solution of the ClO₄⁻ salt with the dimer prepurified by chromatography on a Sephadex LH-20 chromatograph. The purity of the product was verified by a comparison of the electrochemical and electronic spectral features with the literature results.² **Caution!** Perchlorate salts are hazardous due to the possibility of explosion! Complexes should be prepared in small amounts and stored appropriately.

Measurements. pH measurements were conducted by using a calibrated Accumet AB15 pH meter. UV–visible spectra were recorded on either an Agilent 8453 diode-array spectrophotometer or a Shimadzu model UV-3600 UV–visible–near-IR spectrophotometer, both with 2 nm resolution.

Resonance Raman (RR). RR spectra were measured by using continuous-wave excitation at 514.5, 501.7, 496.5, 465.8, and 457.9 nm from a Spectra-Physics 165 Ar⁺ laser and at 676.4, 647.1, and 568.2 nm from a Coherent INNOVA 90K Kr⁺ laser. The incident radiation was collected in a 135° backscattering geometry and dispersed by a

Jobin-Yvon U1000 double monochromator with an 1800 grooves/mm grating. Slits were adjusted for each excitation wavelength to maintain a resolution of 4 cm^{-1} . The Raman signal was detected by a Hamamatsu R943-02 cooled photomultiplier tube with signal processing by an Instruments SA Spectra Link photon-counting system. Samples were prepared in Nanopure water adjusted to pH = 1 with H₂SO₄. As noted above, 0.5 M Na₂SO₄ was used as an internal Raman standard. The concentration of *cis,cis*-[(bpy)₂(H₂O)-Ru^{III}ORu^{III}(OH₂)(bpy)₂]⁴⁺ in water at pH = 1 was 0.2 mM for excitation at 568.2, 647.1, and 676.4 nm and 0.4 mM for the remaining excitation wavelengths. The difference in concentration was necessary because of the difference in absorbance at the different excitation wavelengths. Final spectra were the average of four to nine accumulations.

Spectra were corrected for detector response by using a 200 W Optronics Laboratory OL220M, M-447 quartz–halogen–tungsten lamp operated at 65 A. Corrections for self-absorption of the scattered light were performed by using the method of Myers.¹⁷ Spectral intensities (areas) were determined by using the fitting routines of GRAMS (Galactic Industries). Intensity values were normalized to the sulfate band at 982 cm^{-1} .

Magnetism. Magnetic measurements over the temperature range of 2–350 K (with measurement upon warming after cooling to 2 K in zero field) were made by using a Quantum Design superconducting quantum interference device (SQUID) magnetometer. The dependence of magnetization on the magnetic field ($H = 0$ –7 T) was also verified at 2, 10, 50, and 300 K [data available in the Supporting Information (SI), Figure S1]. The powder sample was tightly packed between thin polymeric disks inside a plastic straw. Diamagnetic contributions to magnetization from the disks and straw were measured independently and subtracted from the total measured signal. The resulting estimated error in the sample magnetization is $\pm 3\%$. The magnetic susceptibility, defined as the sample magnetization (M) divided by the applied magnetic field (H), was determined as a function of the temperature. Effective magnetic moments were calculated as $\mu_{\text{eff}} = 2.828(\chi T)^{1/2}$, where χ is the magnetic susceptibility per formula unit. Susceptibility corrections for the underlying diamagnetism of sample constituents were made using tabulated Pascal's constants.

Computation. DFT calculations were carried out by using *Gaussian* 03, revision C.02.¹⁸ For Gaussian calculations, Becke's three-parameter hybrid functional with the LYP correlation functional (B3LYP) was used with the Los Alamos effective core potential LANL2DZ basis set. The X-ray structure of the blue dimer cation was used as the input in calculations, and initial geometry optimizations of hydrogen-bonded water molecules and chloride anions, when applicable, were performed with *Titan* using Becke's 1988 functional with the Slater exchange and Perdew's 1986 gradient corrections along with his 1981 local correlation functional (BP86) while the blue dimer was frozen. These geometries obtained from *Titan* were used as input geometries for *Gaussian*, where full geometry optimizations were performed at the B3LYP level. Molecular orbital (MO) diagrams were constructed for the fully optimized geometries in Gaussian. Franck–Condon vertical excitation energies and oscillator strengths were obtained with time-dependent DFT (TD-DFT) as implemented in *Gaussian*.

Solvent-specific interactions were modeled by explicitly adding hydrogen-bonded water molecules and chloride anions, respectively. The bulk of the solvent was modeled by means of the integral equation formalism polarizable continuum model (IEF-PCM), as implemented in *Gaussian*.

RESULTS

Magnetism. The variable-temperature magnetic susceptibility of the blue dimer, $[(\text{bpy})_2(\text{H}_2\text{O})\text{Ru}^{\text{III}}\text{ORu}^{\text{III}}(\text{OH}_2)(\text{bpy})_2](\text{ClO}_4)_4$, in magnetic fields of 1000 G (0.10 T) and 10 000 G (1.0 T) is shown in Figure 1. The data clearly exhibit

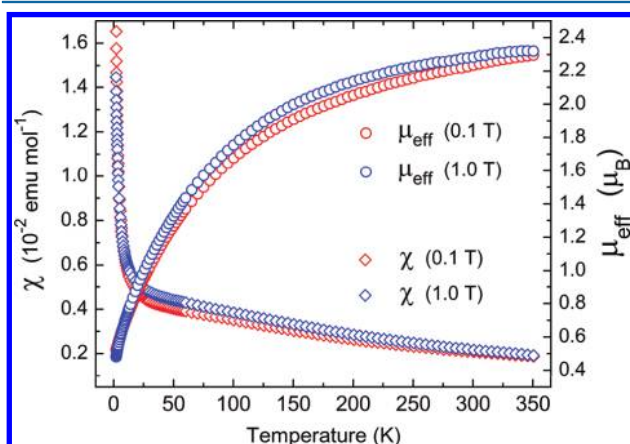


Figure 1. Temperature dependence of χ (magnetic susceptibility per formula unit) and of μ_{eff} (magnetic moment per formula unit) for the blue dimer, $[(\text{bpy})_2(\text{H}_2\text{O})\text{Ru}(\mu\text{-O})\text{Ru}(\text{OH}_2)(\text{bpy})_2](\text{ClO}_4)_4$ in magnetic fields of 1000 G (0.10 T) and 10 000 G (1.0 T).

antiferromagnetic behavior with a steady, approximately linear decrease in the susceptibilities in the range of $\sim 25\text{--}350$ K. The steep increase at temperatures below 20 K is typically associated with the presence of small amounts of paramagnetic impurities. At 350 K, the dimer is paramagnetic with an effective magnetic moment, μ_{eff} of $2.3 \mu_{\text{B}}$ /dimer ($\chi T = 0.66 \text{ emu K mol}^{-1}$). The blue dimer is also paramagnetic in solution at room temperature, as shown by ^1H NMR spectroscopy.¹⁹ In the solid state, χ is temperature-dependent, with μ_{eff} decreasing rapidly as the temperature is lowered below 100 K (Figure 1). The residual magnetic moment of $0.48 \mu_{\text{B}}$ /dimer ($\chi T = 2.8 \times 10^{-2} \text{ emu K mol}^{-1}$) indicates that the blue dimer is essentially diamagnetic at 2 K, although it becomes gradually paramagnetic as the temperature increases. The extrapolated number of unpaired electrons per dimer is only 1.5 even for the highest observed values of μ_{eff} at 350 K.

Similar magnetic measurements were additionally performed for the hexafluorophosphate salt of the blue dimer, $[(\text{bpy})_2(\text{H}_2\text{O})\text{Ru}^{\text{III}}\text{ORu}^{\text{III}}(\text{OH}_2)(\text{bpy})_2](\text{PF}_6)_4$. The data are available as SI (Figure S2), and the corresponding results are nearly identical with those presented above for the perchlorate salt.

UV–Visible–Near-IR Spectra. The spectrum of the diaqua ruthenium dimer, $[(\text{H}_2\text{O})\text{Ru}^{\text{III}}\text{ORu}^{\text{III}}(\text{OH}_2)]^{4+}$, is shown in Figure 2. It is blue, with the most intense absorption feature in the visible appearing at 637 nm at pH = 1. The spectrum is pH-dependent, with significant shifts in absorption occurring at higher pHs, where the dominant forms become $[(\text{H}_2\text{O})\text{Ru}^{\text{III}}\text{ORu}^{\text{III}}(\text{OH})]^{3+}$ and $[(\text{HO})\text{Ru}^{\text{III}}\text{ORu}^{\text{III}}(\text{OH})]^{2+}$.

The UV–visible spectra of *cis,cis*- $[(\text{bpy})_2(\text{H}_2\text{O})\text{Ru}^{\text{III}}\text{ORu}^{\text{III}}(\text{OH}_2)(\text{bpy})_2]^{4+}$, *cis,cis*- $[(\text{bpy})_2(\text{Cl})\text{Ru}^{\text{III}}\text{ORu}^{\text{III}}(\text{Cl})(\text{bpy})_2]^{2+}$, and related μ -oxo-bpy complexes are dominated by a manifold of intense $d\pi \rightarrow \pi^*(\text{bpy})$ and $\pi \rightarrow \pi^*(\text{bpy})$ absorptions in the UV, with additional bands appearing in the low-energy visible. For *cis,cis*- $[(\text{bpy})_2(\text{Cl})\text{Ru}^{\text{III}}\text{ORu}^{\text{III}}(\text{Cl})(\text{bpy})_2]^{2+}$ in acetonitrile, the visible λ_{max} appears at 672 nm ($\epsilon = 17\,900 \text{ M}^{-1} \text{ cm}^{-1}$).⁷

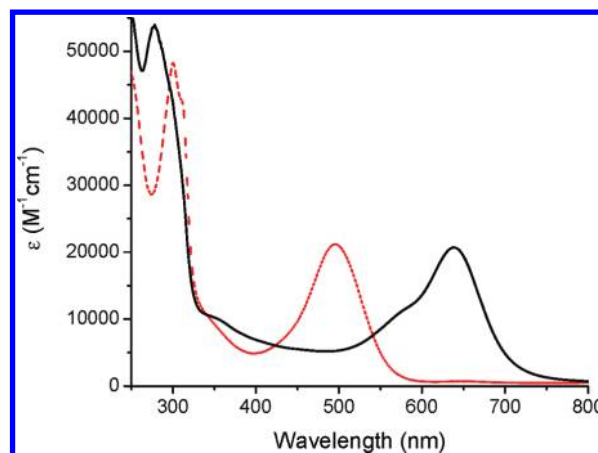


Figure 2. UV–visible spectra for $[(\text{bpy})_2(\text{H}_2\text{O})\text{Ru}^{\text{III}}\text{ORu}^{\text{III}}(\text{OH}_2)(\text{bpy})_2]^{4+}$ (black, solid) and $[(\text{bpy})_2(\text{HO})\text{Ru}^{\text{IV}}\text{ORu}^{\text{III}}(\text{OH}_2)(\text{bpy})_2]^{4+}$ (red, dashed) in 0.1 M HNO_3 .

There is a shoulder on the high-energy side of the intense absorption band in these complexes that is readily apparent. The overlapping absorption features exhibit different solvent dependences. For *cis,cis*- $[(\text{bpy})_2(\text{Cl})\text{Ru}^{\text{III}}\text{ORu}^{\text{III}}(\text{Cl})(\text{bpy})_2]^{2+}$, shifts in λ_{max} are observed in nine solvents (water, ethanol, methanol, acetonitrile, propylene carbonate, dichloromethane, dimethyl sulfoxide, acetone, and benzyl alcohol) from 654 nm in water to 674 nm in benzyl alcohol. Representative spectra are shown in the SI, Figure S3. Assignments of these and other absorption features, consistent with RR excitation profiles and the results of DFT calculations, are presented below.

Broad absorptions with low molar extinction coefficients are observed in the near-IR for the blue dimer and its higher-oxidation-state forms (Figure 3). In this region, $d\pi \rightarrow d\pi$ interconfigurational (IC) transitions appear for partly filled $d\pi$ sublevels such as $\text{Ru}^{\text{III}} d\pi$.²⁰

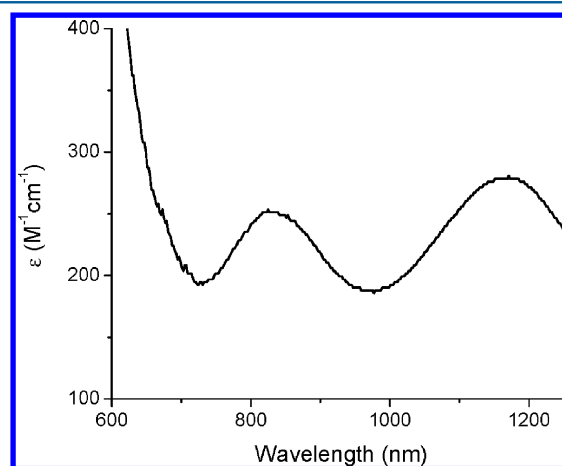


Figure 3. Near-IR absorption spectrum of *cis,cis*- $[(\text{bpy})_2(\text{HO})\text{Ru}^{\text{IV}}\text{ORu}^{\text{III}}(\text{OH}_2)(\text{bpy})_2]^{4+}$ in 0.1 M DNO_3 at room temperature.

These absorption bands are pH-dependent and exhibit distinguishable shifts with changes in the oxidation state or

coordination environment, which has proven useful in identifying intermediates and monitoring reactions in catalytic water oxidation cycles.⁶ Near-IR absorption band energies for the Ru^{III}ORu^{III} and Ru^{IV}ORu^{III} forms of the blue dimer are listed in Table 1.

Table 1. Near-IR Absorption Bands for the Ru^{III}ORu^{III} and Ru^{IV}ORu^{III} Forms of the Blue Dimer in Water

complex cation	nm (cm ⁻¹)	ϵ (M ⁻¹ cm ⁻¹)
[(H ₂ O)Ru ^{III} ORu ^{III} (OH ₂) ⁴⁺	1133 (8830)	380
[(H ₂ O)Ru ^{III} ORu ^{III} (OH)] ³⁺	1103 (9070)	370
[(H ₂ O)Ru ^{IV} ORu ^{III} (OH ₂) ⁵⁺	840 (11 900)	230
	1182 (8460)	300
[(HO)Ru ^{IV} ORu ^{III} (OH ₂) ⁴⁺	832 (12 000)	250
	1164 (8590)	280

Excitation-Dependent RR. Excitation-dependent RR measurements were conducted on *cis,cis*-[(bpy)₂(H₂O)-Ru^{III}ORu^{III}(OH₂)(bpy)₂]⁴⁺ in a pH = 1 aqueous medium at room temperature to assist in the assignment of the absorption spectra. In this experiment, resonance enhancements are observed only for totally symmetric modes for which there is a change in the equilibrium displacement, $\Delta Q_{\text{eq}} \neq 0$. In principle, analysis of the excitation-dependent profiles provides quantitative information, both frequencies and displacements, on a mode-by-mode basis and is useful in assigning underlying electronic transitions.^{21–25} The blue dimer spectrum consists of a heavily overlapped series of absorptions obviating quantitative analysis, but the observed trends assist in assigning the underlying electronic transitions.

Figure 4 shows a typical RR spectrum obtained with 514.5 nm excitation in water at pH = 1, with assignments given in Table 2. The bpy bands are labeled according to the nomenclature used in the normal-coordinate analysis by Kincaid and co-workers for [Ru(bpy)₃]²⁺.^{26,27}

Table 2. Raman Band Energies, Polarizations (Polarized, P; Depolarized, dp), and Proposed Assignments for [(bpy)₂(H₂O)Ru^{III}ORu^{III}(OH₂)(bpy)₂]⁴⁺ in Water at pH = 1

Raman shift (cm ⁻¹)	polarization	assignment
133	P	$\delta_{\text{sym}}(\text{Ru}-\text{O}-\text{Ru})$
170	dp	$\nu(\text{bpy})$
213	dp	
236	P	$\nu(\text{Ru}-\text{N})$
254		$\nu(\text{bpy})$
298	P	$\nu_{19}(\text{bpy})$
342	P	$\nu(\text{bpy})$
364		$\nu_{18}(\text{bpy})$
390	P	$\nu_{\text{sym}}(\text{Ru}-\text{O}-\text{Ru})$
419		
436	dp	
461	P	$\nu(\text{bpy})$
487	P	
551	P	$\nu_{\text{sym}}(\text{Ru}-\text{O}-\text{Ru}) + 170$
606		$\nu_{\text{sym}}(\text{Ru}-\text{O}-\text{Ru}) + 254$
666		$\nu_{17}(\text{bpy})$
728		$\nu_{\text{sym}}(\text{Ru}-\text{O}-\text{Ru}) + 342$
765		$2\nu_{\text{sym}}(\text{Ru}-\text{O}-\text{Ru}), \nu(\text{bpy})$
820		$\nu_{\text{asym}}(\text{Ru}-\text{O}-\text{Ru})$
1040		$\nu_{15}(\text{bpy})$
1111		$\nu_{13}(\text{bpy})$
1176		$\nu_{12}(\text{bpy})$
1278		$\nu_{10}(\text{bpy})$
1319		$\nu_9(\text{bpy})$
1494		$\nu_7(\text{bpy})$
1562		$\nu_6(\text{bpy})$
1604		$\nu_5(\text{bpy})$

There are features of interest in these data. 647.1 nm (15 400 cm⁻¹) Excitation: Excitation at this wavelength occurs within the absorption manifold of the intense band at 637 nm. In the

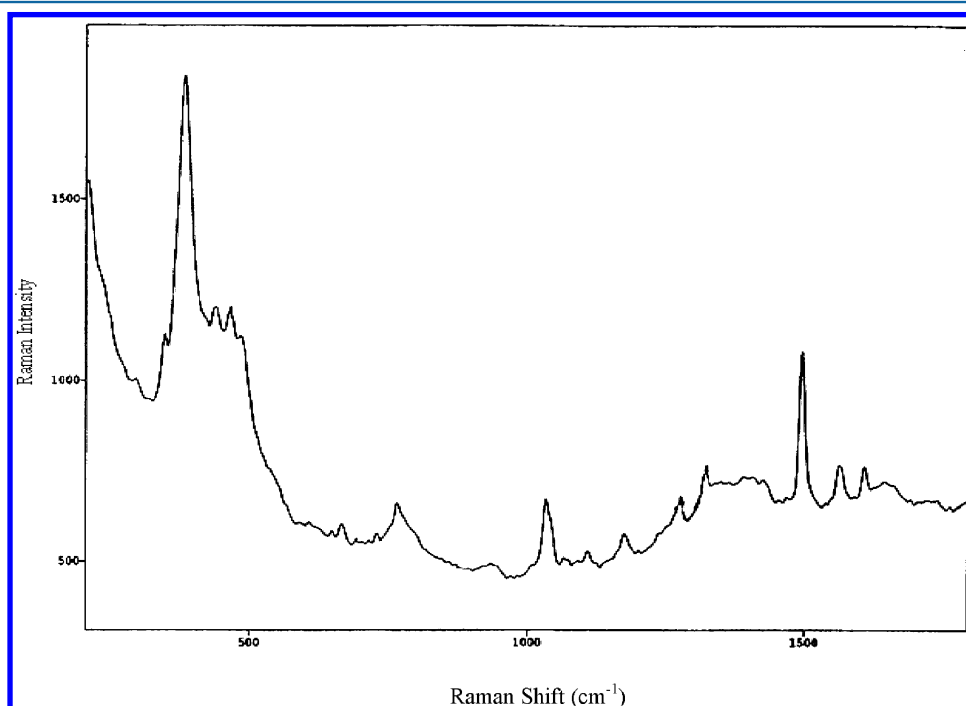


Figure 4. RR spectrum of [(bpy)₂(H₂O)Ru^{III}ORu^{III}(OH₂)(bpy)₂]⁴⁺ in aqueous H₂SO₄ at pH = 1 with 514.5 nm excitation at room temperature.

Table 3. Differential Raman Cross Sections at Various Excitation Wavelengths for $[(\text{bpy})_2(\text{H}_2\text{O})\text{Ru}^{\text{III}}\text{ORu}^{\text{III}}(\text{OH}_2)(\text{bpy})_2]^{4+}$ in Water at pH = 1

band (cm^{-1})	laser excitation wavelength (nm)									
	457.6	465.8	476.5	488.0	496.5	501.7	514.5	568.2	647.1	676.4
298	16.4	15.8	34.4	45.8	36.7	19.4	6.6	0	24.5	0
342	77.1	135.0	187.7	211.1	229.8	81.4	14.1	0	182.4	80.0
364	0	0	0	0	0	0	26.6	0	2283	3087
390	939.5	252.7	1156	1158	1537	745.5	663.0	172.0	8556	2932
436	638.7	661.7	809.6	686.3	588.0	528.9	319.6	329.6	598.3	636.0
461	190.9	130.8	134.1	202.9	235.4	81.0	60.1	82.4	627.3	305.1
487	156.5	303.7	324.8	138.9	226.8	223.4	516.1	0	643.4	110.5
606	121.0	366.6	598.6	333.4	12.5	13.2	0	0	0	0
666	13.9	20.5	25.0	60.1	24.0	13.2	5.8	0	0	0
1040	307.1	293.0	275.4	289.0	215.5	163.7	124.3	0	661.0	286.0
1111	129.5	131.0	139.2	21.6	116.7	58.0	78.9	0	199.4	159.4
1176	59.2	54.5	52.4	32.7	48.8	22.8	19.6	0	176.0	225.2
1278	89.0	91.1	90.3	87.2	88.5	88.0	30.0	10.5	392.0	130.6
1319	78.8	72.5	0	0	92.4	38.1	48.0	0	40.0	41.9
1494	198.0	216.6	0	164.0	185.4	186.9	162.9	61.8	90.2	87.5
1562	65.5	105.9	95.0	41.9	62.8	60.0	76.1	0	96.3	0
1604	76.4	123.4	0	78.8	40.9	31.0	31.3	0	20.1	67.5

100–500 cm^{-1} region, the spectrum is dominated by an intense band near 385 cm^{-1} with 14 additional bands enhanced. The 385 cm^{-1} band has been assigned to the symmetric Ru–O–Ru stretch of the bridge, $\nu_{\text{sym}}(\text{Ru–O–Ru})$.⁸ Above 500 cm^{-1} , overtones and combination bands that are of low intensity arise from a mixture of $\nu_{\text{sym}}(\text{Ru–O–Ru})$ and a series of bands arising from ring vibrations of the bpy ligand. Note the band assignments in Table 2.

The vibrational mode $\nu_{18}(\text{bpy})$ at 364 cm^{-1} , and to a lesser degree $\nu(\text{bpy})$ bands at 436, 461, and 1040 cm^{-1} , is also resonantly enhanced. All of these low-frequency $\nu(\text{bpy})$ bands have significant Ru–N character. It is also notable that, in a relative sense, medium-frequency $\nu(\text{bpy})$ ring stretching modes at 1111, 1176, and 1278 cm^{-1} are enhanced upon excitation at 647.1 and 674.1 nm.

514.5 nm (1940 cm^{-1}) Excitation: Upon 514.5 nm excitation, $\nu_{\text{sym}}(\text{Ru–O–Ru})$ is also strongly enhanced. Absorption at this wavelength is dominated by the absorptions at 580 and 480 nm. Other bands are comparably enhanced, including bands of $\nu(\text{bpy})$ origin (Table 3).

457.6 cm^{-1} (21800 cm^{-1}) Excitation: Absorption at this wavelength is also dominated by the absorption bands at 580 and 480 nm. In a relative sense, $\nu(\text{bpy})$ bands at 1040, 1111, 1176, 1278, 1319, 1494, and 1562 cm^{-1} are increasingly enhanced as the excitation energy is increased from 514.5 to 457.6 nm. Resonance enhancement of these bands is reminiscent of enhancements found for Ru \rightarrow bpy metal-to-ligand charge-transfer (MLCT) excitation in complexes such as $[\text{Ru}(\text{bpy})_3]^{2+}$.²⁸

Parts a and b of Figure 5 show Raman excitation profiles for representative bands at 364, 390, 461, 487, and 1040 cm^{-1} . On the basis of the Kincaid analysis, these bands are assigned to $\nu_{18}(\text{bpy})$, $\nu_{\text{sym}}(\text{Ru–O–Ru})$, $\nu(\text{bpy})$, and $\nu_{15}(\text{bpy})$. Differential Raman cross sections for each Raman band at different excitation wavelengths are listed in Table 3.

DFT Calculations. The electronic structure of the blue dimer has been investigated theoretically by application of CASSCF calculations¹¹ and DFT with application of the broken-symmetry approximation.¹² These calculations predict a relatively small extent of electronic coupling across the Ru–O–

Ru bridge. We find that the results of these calculations are of limited value because they fail to account for the extensive experimental data available for this molecule. The results of DFT calculations based on the experimentally observed singlet ground state, which were described elsewhere in a preliminary form,¹⁶ are extended here. They successfully account for both key chemical properties and electronic and molecular structures.

Geometries. *cis,cis-[(bpy)₂(H₂O)Ru^{III}ORu^{III}(OH₂)(bpy)₂]⁴⁺.* The coordinates from the X-ray structure of $[(\text{bpy})_2(\text{H}_2\text{O})\text{Ru}^{\text{III}}\text{ORu}^{\text{III}}(\text{OH}_2)(\text{bpy})_2]^{4+}$ (PDB file) were used as the input geometry for *Gaussian*. Although two geometric isomers are possible, all known X-ray structures for the family $[(\text{bpy})_2(\text{L})\text{RuORu}(\text{L})(\text{bpy})_2]^{n+}$ (L = H₂O, Cl, NO₂, NH₃) are for the enantiomeric isomeric pair, and the results reported here focused on that structure. The ground state was assumed to be a singlet, consistent with the known magnetic properties, and the structure was optimized at the DFT level (B3LYP and LANL2DZ) with no symmetry restrictions.

Tight convergence criteria were used for both the self-consistent field and optimization itself. The calculation converged to final C₂ symmetry, which was used to calculate the gas-phase absorption spectrum and to build outer-coordination-sphere structures with hydrogen-bonded water molecules and counterions. A delocalized electronic model with strong coupling was first proposed by Dunitz and Orgel for $[\text{Cl}_3\text{RuORuCl}_3]^{4-}$ and later modified for the blue dimer.^{7,29} A related analysis was reported for μ -oxoiron porphyrin dimers by Tatsumi and Hoffmann.³⁰ We have extended our earlier DFT results based on a closed-shell singlet ground state by using the B3LYP functional and LANL2DZ basis set as implemented in *Gaussian03*.

Table 4 compares selected bond distances and angles for the reported X-ray diffraction (XRD) structure of *cis,cis-[(bpy)₂(H₂O)Ru^{III}ORu^{III}(OH₂)(bpy)₂](ClO₄)₄* and optimized geometries for the cation in the gas phase and with water molecules and/or chloride counteranions.

cis,cis-[(bpy)₂(H₂O)Ru^{III}ORu^{III}(OH₂)(bpy)₂]⁴⁺·4H₂O (BD·4H₂O). Two water molecules were hydrogen-bonded to each of the two aqua ligands in the optimized gas-phase

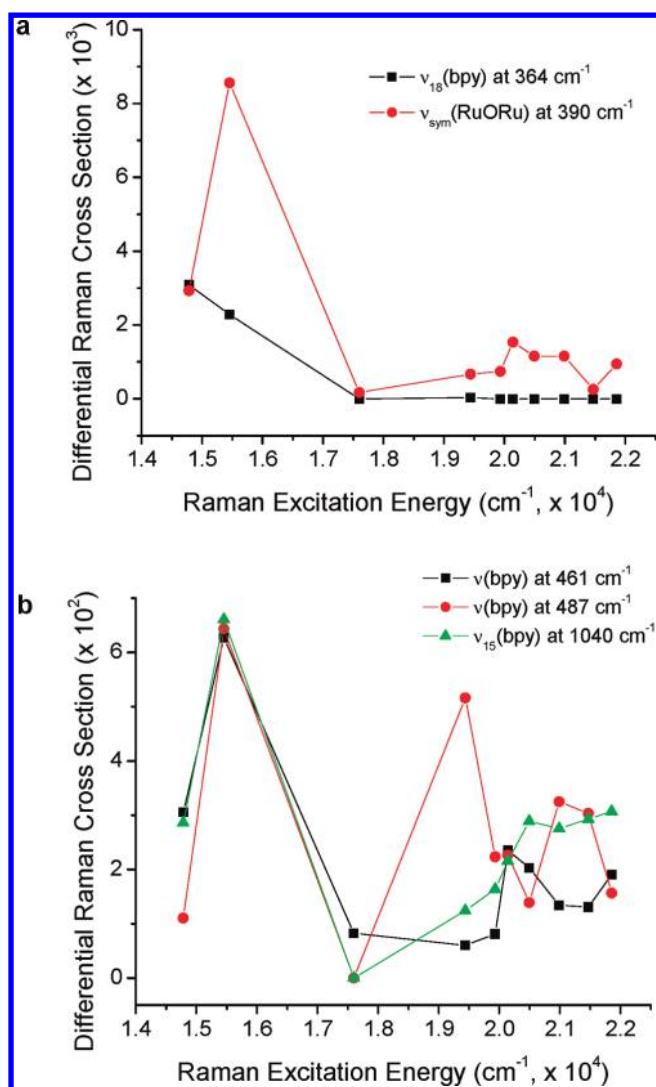


Figure 5. (a) Raman excitation profiles for $cis,cis-[(bpy)_2(H_2O)Ru^{III}ORu^{III}(OH_2)(bpy)_2]^{4+}$ in water at pH = 1 vs 0.5 M Na_2SO_4 for $\nu_{sym}(Ru-O-Ru)$ at 390 cm^{-1} and $\nu_{18}(bpy)$ at 364 cm^{-1} . (b) Raman excitation profiles for $cis,cis-[(bpy)_2(H_2O)Ru^{III}ORu^{III}(OH_2)(bpy)_2]^{4+}$ in water at pH = 1 vs 0.5 M Na_2SO_4 for $\nu(bpy)$ at 461 cm^{-1} , $\nu(bpy)$ at 487 cm^{-1} , and $\nu_{15}(bpy)$ at 1040 cm^{-1} . Note the band assignments are given in Table 2.

Table 4. Significant Bond Distances and Angles from the XRD and Optimized Geometries of the Blue Dimer with Different Numbers of Water Molecules and Chloride Ions in the Outer Coordination Sphere

metric feature	exp	BD	BD·4H ₂ O	BD·12H ₂ O	BDCl ₄ ·4H ₂ O
$d(Ru-O_{oxo})$, Å	1.869	1.928	1.923	1.911	1.905
$d(Ru-O_{aqua})$, Å	2.137	2.236	2.157	2.127	2.112
$d(Ru-N)$, Å	2.056	2.100	2.104	2.099	2.091
$\angle Ru-O-Ru$	165.5	158.3	162.2	160.9	162.3

structure with a hydrogen-bond distance of 1.500 Å, and the resulting “hydrate” was fully optimized under C_2 symmetry.

$cis,cis-[(bpy)_2(H_2O)Ru^{III}ORu^{III}(OH_2)(bpy)_2]^{4+} \cdot 12H_2O$ (BD·12H₂O). Two additional water molecules were hydrogen-bonded to each of the four hydrogen-bonded water molecules in BD·4H₂O to complete a total of 12 hydrogen-bonded water molecules. The resulting structure was fully optimized under C_2 symmetry.

$cis,cis-[(bpy)_2(H_2O)Ru^{III}ORu^{III}(OH_2)(bpy)_2](Cl)_4 \cdot 4H_2O$ (BDCl₄·4H₂O). Four chloride anions were added to BD·4H₂O, each hydrogen-bonded to one of the four hydrogen-bonded water molecules with a hydrogen-bond distance of 1.700 Å. The resulting structure was fully optimized under C_2 symmetry. (Optimized structure illustrations are provided in the SI.)

A DFT-calculated energy-level diagram is shown in Figure 6. Important features include the following: (i) The highest filled

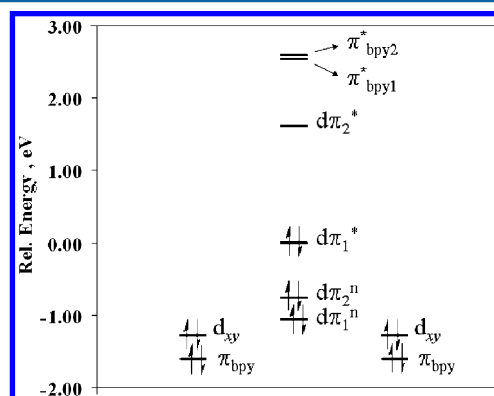


Figure 6. Energy-level diagram for $cis,cis-[(bpy)_2(H_2O)Ru^{III}ORu^{III}(OH_2)(bpy)_2]^{4+}$ from DFT calculations based on the B3LYP functional and LANL2DZ basis set. A closed-shell singlet ground state was assumed. The energy levels are labeled to indicate their dominant orbital compositions, with $d\pi_1^*$ and $d\pi_2^*$ largely antibonding $d\pi$ in character arising from $d\pi-2p_{\pi,O}-d\pi$ mixing. Levels $d\pi_1^n$ and $d\pi_2^n$ are the corresponding nonbonding pair. The $d\delta$ (d_{xy}) orbitals are largely localized at each Ru and have δ symmetry with regard to the Ru- μ -O bonds. Reprinted with permission from ref 6. Copyright 2008 American Chemical Society.

molecular level, $d\pi_1^*$, is antibonding and largely $d\pi$ in character and is formed predominantly from $d\pi-2p_{\pi,O}-d\pi$ mixing. (ii) The lowest unoccupied level, $d\pi_2^*$, is similarly antibonding with regard to the Ru-O-Ru $d\pi-p\pi$ interaction. (iii) The Ru-O-Ru $d\pi-p\pi$ interaction also gives rise to filled bonding levels, not shown, which are largely $2p_{\pi,O}$ in character, and a nonbonding pair $d\pi_1^n-d\pi_2^n$. (iv) The remaining $d\pi$ orbitals, $d\delta$ (d_{xy}), are largely localized at each Ru and have δ symmetry with regard to the Ru- μ -O bonding axes defined as the z axis at each Ru.

TD-DFT calculations on the optimized structures provide a basis for interpreting the UV-visible absorption spectrum of the blue dimer. The introduction of hydrogen-bonded water molecules and counterions significantly improves excitation energies, although the overall shape of the absorption envelope is well accounted for with a PCM for the solvent. A spectrum recorded at pH = 1 and assignments based on the orbital diagram in Figure 6 are shown in Figure 7.

On the basis of these assignments, the visible absorption band that accounts for the blue in the blue dimer arises from overlapping $d\pi \rightarrow \pi_{bpy}^*$ (MLCT) and bridge-based $d\pi \rightarrow d\pi^*$ transitions. The DFT calculations predict three low-lying bands arising from transitions that have IC $d\pi \rightarrow d\pi$ character. Low-energy absorption features in the spectrum at 1205, 1125, and 915 nm ($\epsilon = 200-400 M^{-1} cm^{-1}$) are assigned to IC transitions within the $d\pi$ orbital set, $d_{xy}, d\pi_n \rightarrow d\pi_2^*$ (Table 1). These three absorptions originate from two sets of d_{xy} orbitals, which have δ symmetry with regard to the Ru-O-Ru bridge, and $d\pi_{1n}$, the higher-energy nonbonding level arising from the through-bridge interaction. The acceptor level is $d\pi_2^*$, the

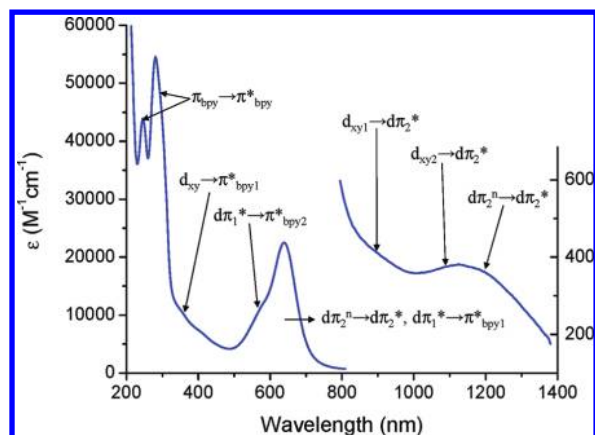


Figure 7. UV-visible-near-IR spectrum of *cis,cis*-[(bpy)₂(H₂O)-Ru^{III}ORu^{III}(OH₂)(bpy)₂]⁴⁺ in water at pH = 1. Band assignments are based on the bonding scheme in Figure 8. $\epsilon = 21\,100\text{ M}^{-1}\text{ cm}^{-1}$ for the intense band at 637 nm. Adapted from Figure 10 of ref. 6. Copyright 2008 American Chemical Society.

second of two antibonding levels, largely $d\pi$ in character but mixed with $2p_{\text{O}}$. The oscillator strengths ($f \leq 0.0003$) are low for these bands, consistent with the IC $d\pi \rightarrow d\pi$ character of the transitions.

Table 5 presents proposed UV-visible band assignments for [(bpy)₂(H₂O)Ru^{III}ORu^{III}(OH₂)(bpy)₂]⁴⁺ based on the orbital

Table 5. Absorption Band Energies and Proposed Assignments for *cis,cis*-[(bpy)₂(H₂O)Ru^{III}ORu^{III}(OH₂)(bpy)₂]⁴⁺ in Water at pH = 1 (See the Text)

absorption band (nm)	ϵ (M ⁻¹ cm ⁻¹)	assignment
271	46 875	$\pi \rightarrow \pi^*(\text{bpy})$
280	54 480	$\pi \rightarrow \pi^*(\text{bpy})$
375	8 795	$d\pi_1^*, d\pi_n \rightarrow \pi^*(\text{bpy})$ (MLCT)
410	6 960	$d\pi_2^n \rightarrow \pi^*(\text{bpy})$ (MLCT)
480	4 215	$\pi_1 \rightarrow d\pi_2^*, \pi_2 \rightarrow d\pi_2^*$ (LMCT)
580	11 930	$d\pi_2^n \rightarrow d\pi_2^*, d\pi_1^* \rightarrow \pi_2^*$ ($d\pi^n \rightarrow d\pi^*$; MLCT)
637	22 500	$d\pi_2^n \rightarrow d\pi_2^*, d\pi_1^* \rightarrow \pi_2^*$ ($d\pi^n \rightarrow d\pi^*$; MLCT)
1133	380	$d_{xy1} \rightarrow d\pi_2^*, d_{xy2} \rightarrow d\pi_2^*, d\pi_2^n \rightarrow d\pi_2^*$

designations in Figure 6. They are consistent with the excitation-dependent RR data and the results of the DFT calculations. Figure 8 illustrates MOs for [(bpy)₂(H₂O)Ru^{III}ORu^{III}(OH₂)(bpy)₂]⁴⁺ involved in electronic transitions in the near-IR and visible.

Both optimized geometries and electronic spectra for [(bpy)₂(H₂O)Ru^{III}ORu^{III}(OH₂)(bpy)₂]⁴⁺ were obtained in the DFT calculations. Calculations based on C₂ symmetry reproduced the overall profile of the experimental spectrum (Figure 9). The visible λ_{max} was red-shifted by ~70 nm in the gas-phase spectrum relative to the experimental value in solution at pH = 1. With the IEF-PCM model and acetonitrile as the solvent, $\lambda_{\text{max}} = 505$ nm for the bridge-based band in the calculated spectrum of [(bpy)₂(OH)Ru^{IV}ORu^{III}(OH₂)(bpy)₂]⁴⁺ matches well with the experimental value, $\lambda_{\text{max}} = 513$ nm (see the SI, Figure S5). Under the conditions of the experiment, solvent exchange with the aqua ligands is known to be slow.⁹

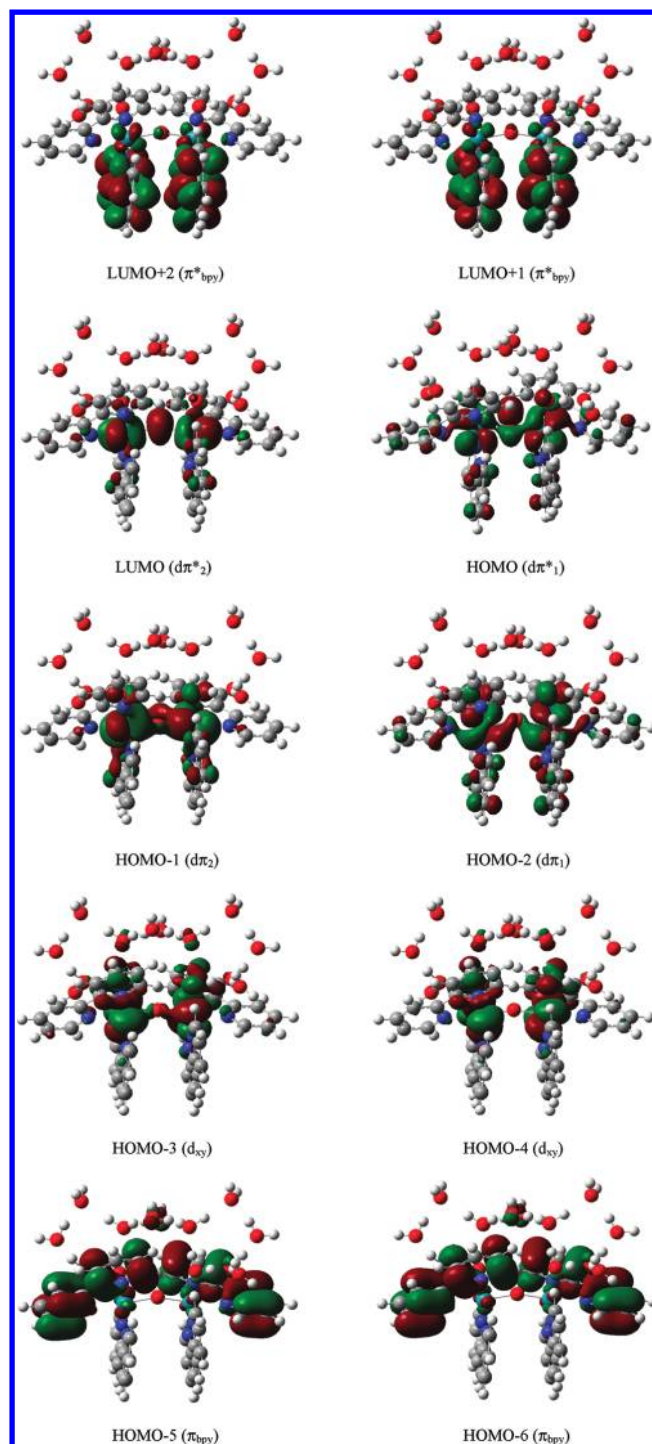


Figure 8. MOs for [(bpy)₂(H₂O)Ru^{III}ORu^{III}(OH₂)(bpy)₂]⁴⁺ involved in MLCT and bridge-based electronic transitions in the near-IR-visible.

A dramatic improvement in the calculated absorption spectrum is observed with inclusion of specific water molecules and counteranions, or non-hydrogen-bonding solvents, with application of the IEF-PCM model. Further illustration of this point is given in the SI, Figure S6, where an exceptional match between the calculated and experimental absorption spectra of *cis*-Ru(bpy)₂Cl₂ is observed. The IEF-PCM model with water as the solvent was successfully used in this calculation because of the absence of sites on the chloro ligands for specific hydrogen-bonding interactions. Related TD-DFT results

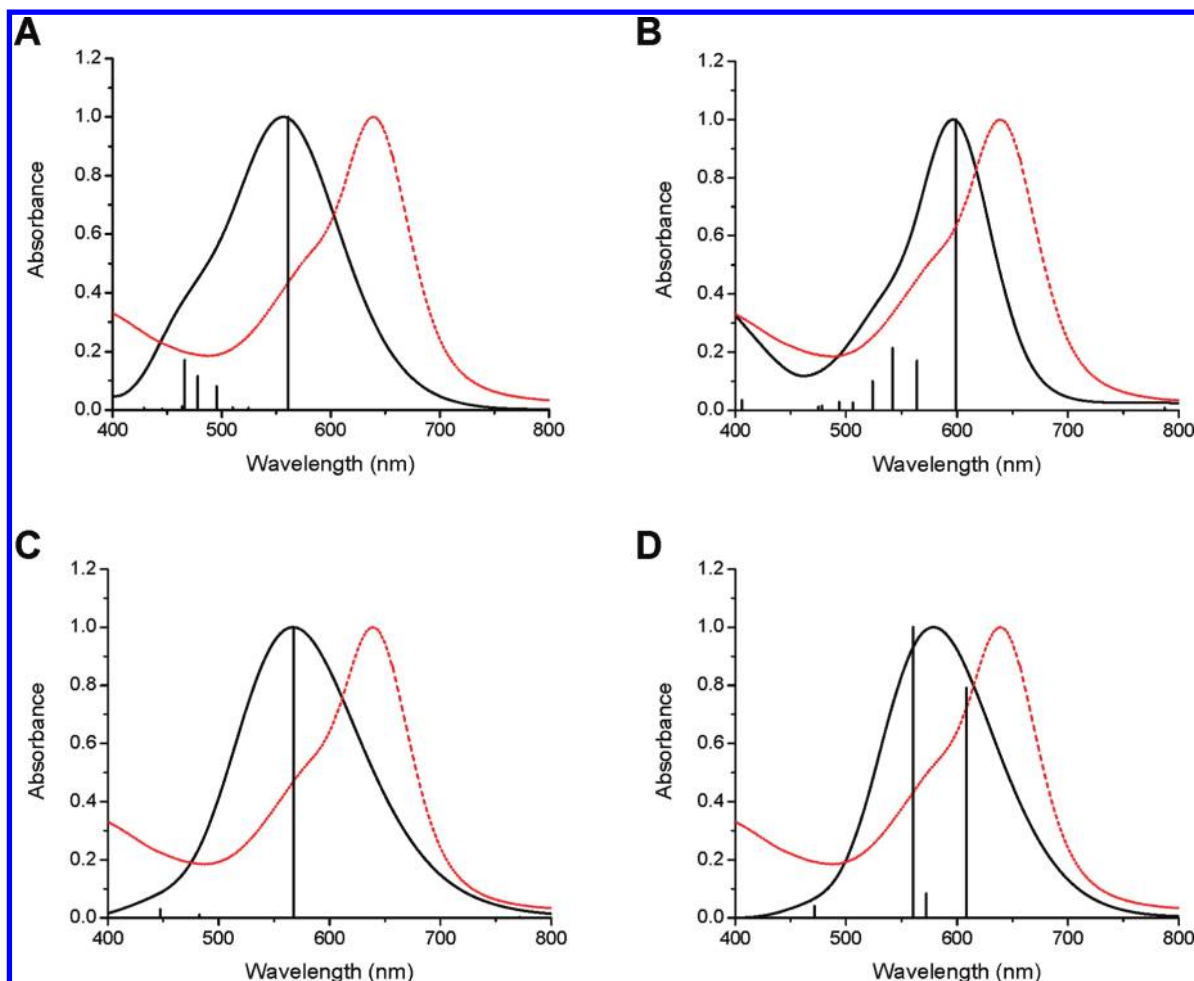


Figure 9. Comparison of the normalized theoretical and experimental absorption spectra for the blue dimer: (A) strong coupling, BD; (B) strong coupling, $\text{BDCl}_4 \times 4\text{H}_2\text{O}$; (C) triplet electronic state; (D) broken symmetry (BS-BD). Gaussian-broadened theoretical spectra are in black, with their underlying individual transitions superimposed. The experimental spectrum is shown with a red, dashed line.

including structure and solvent effects on calculated absorption spectra have been reported.^{31–33}

Notably absent in the calculated absorption spectra of the blue dimer using the broken-symmetry approximation and triplet electronic state (Figure 9) is the high-energy shoulder found in the experimental spectrum of the visible λ_{max} absorption band. Stick diagrams are provided to show the individual vibronic transitions, giving rise to the corresponding Gaussian-broadened bands of the calculated spectra obtained from TD-DFT of the optimized geometries.

Successful estimation of the redox potentials with DFT calculations is well-documented in the literature.^{12,34} Our DFT results also successfully predict redox potentials in non-hydrogen bonding solvents for non-PCET, one-electron couples. For example, for the $[(\text{bpy})_2(\text{Cl})\text{Ru}^{\text{IV}}\text{ORu}^{\text{III}}(\text{Cl})-(\text{bpy})_2]^{3+}/[(\text{bpy})_2(\text{Cl})\text{Ru}^{\text{III}}\text{ORu}^{\text{III}}(\text{Cl})(\text{bpy})_2]^{2+}$ couple, the experimental⁷ and calculated $E_{1/2}$ values (in CH_3CN , $I = 0.1$, vs NHE) are 0.93 and 0.99, respectively (see the SI for details).

DISCUSSION

The blue dimer, $\text{cis,cis}-[(\text{bpy})_2(\text{H}_2\text{O})\text{Ru}^{\text{III}}\text{ORu}^{\text{III}}(\text{OH}_2)-(\text{bpy})_2]^{4+}$, was the first designed molecular catalyst for water oxidation.^{1,2} The details by which it oxidizes water have been the subject of a series of investigations^{3–6} and will be the subject of a future paper. Oxidative activation of the blue dimer

involves stepwise oxidation through the formal oxidation states $\text{Ru}^{\text{III}}\text{ORu}^{\text{III}}$, $\text{Ru}^{\text{IV}}\text{ORu}^{\text{III}}$, $\text{Ru}^{\text{IV}}\text{ORu}^{\text{IV}}$, and $\text{Ru}^{\text{V}}\text{ORu}^{\text{IV}}$, ultimately to $\text{Ru}^{\text{V}}\text{ORu}^{\text{V}}$. Oxidation increases the acidity of bound protons and PCET, with proton accompanying electron; e.g., $[(\text{bpy})_2(\text{H}_2\text{O})\text{Ru}^{\text{III}}\text{ORu}^{\text{III}}(\text{OH}_2)(\text{bpy})_2]^{4+} - e^- - \text{H}^+ \rightarrow [(\text{bpy})_2(\text{HO})\text{Ru}^{\text{IV}}\text{ORu}^{\text{III}}(\text{OH}_2)(\text{bpy})_2]^{4+}$, allows accumulation of multiple oxidative equivalents without significant charge buildup. PCET is key in allowing the blue dimer to meet the $4e^-/4\text{H}^+$ demands of the oxygen/water half-reaction $2\text{H}_2\text{O} \rightarrow \text{O}_2 + 4\text{H}^+ + 4e^-$.

As noted above, both the blue dimer and its once-oxidized form, $\text{cis,cis}-[(\text{bpy})_2(\text{HO})\text{Ru}^{\text{IV}}\text{ORu}^{\text{III}}(\text{OH}_2)(\text{bpy})_2]^{4+}$, have been characterized structurally. The intermediate state, $\text{Ru}^{\text{IV}}\text{ORu}^{\text{IV}}$, is a transient, unstable toward disproportionation into $\text{Ru}^{\text{IV}}\text{ORu}^{\text{III}}$ and $\text{Ru}^{\text{V}}\text{ORu}^{\text{IV}}$. $\text{Ru}^{\text{V}}\text{ORu}^{\text{IV}}$, $[(\text{bpy})_2(\text{O})\text{Ru}^{\text{V}}\text{ORu}^{\text{IV}}(\text{O})(\text{bpy})_2]^{3+}$ by pH-dependent electrochemical measurements,² exists as a discrete intermediate and undergoes slow water oxidation by a complex mechanism.⁶ The state $\text{Ru}^{\text{V}}\text{ORu}^{\text{V}}$ is a transient intermediate undergoing O-atom transfer to water to give the peroxidic intermediate $[(\text{bpy})_2-(\text{HOO})\text{Ru}^{\text{III}}\text{ORu}^{\text{V}}(\text{O})(\text{bpy})_2]^{4+}$.

The goal of this paper was to examine the electronic structure of the blue dimer, which, as noted in the Introduction, has been a source of controversy. In the original DFT calculations by Baik and co-workers,¹² the ground state was

described as a relatively weakly coupled Ru^{III}–Ru^{III} dimer with magnetic exchange and a singlet ground state. On the basis of DFT (B3LYP) and CASSCF calculations,¹¹ Batista and Martin concluded that the ground state is a weakly antiferromagnetically coupled singlet. They concluded that partial electronic delocalization occurs by mixing between $d\pi$ rather than by $d\delta$ orbitals as concluded by Baik and co-workers.^{11,12}

There is clear evidence for strong electronic coupling in the blue dimer. This cross-bridge $d\pi$ – $p\pi$ – $d\pi$ interaction dominates key properties and distinguishes it from structurally related, monomeric ruthenium(III) complexes.

Structure. Key intramolecular structural details for the cation cis,cis -[(bpy)₂(H₂O)Ru^{III}ORu^{III}(OH₂)(bpy)₂]²⁺ are listed in Table 6, where comparisons are made with the Ru–

Table 6. Comparison of Selected Bond Distances (Å) and Angles (deg) for the Cations in

[(bpy)₂(H₂O)Ru^{III}ORu^{III}(OH₂)(bpy)₂](ClO₄)₄·2H₂O,² [(bpy)₂(H₃N)Ru^{III}ORu^{III}(NH₃)(bpy)₂](ClO₄)₄·2H₂O,¹⁵ and [(bpy)₂(O₂N)Ru^{III}ORu^{III}(NO₂)(bpy)₂](ClO₄)₂·2H₂O.¹⁴

	(H ₂ O)- Ru ^{III} ORu ^{III} - (OH ₂)	(H ₃ N)- Ru ^{III} ORu ^{III} - (NH ₃)	(O ₂ N)- Ru ^{III} ORu ^{III} - (NO ₂)
	Distances		
M(1)–O	1.869(1)	1.8939(15)	1.876(6)
M(2)–O	1.869(1)	1.8939(15)	1.890(7)
L–M(1)	2.136(4) (L = OH ₂)	2.126(6) (L = NH ₃)	2.067(11) (L = NO ₂)
M(2)–L'	2.136(4) (L' = OH ₂)	2.126(6) (L' = NH ₃)	2.034(8) (L = NO ₂)
L···L ^a	4.725 (H ₂ O···OH ₂)	4.816 (H ₃ N···NH ₃)	5.518 (O ₂ N···NO ₂)
	Angles		
L–M(1)–O	89.4(2) (L = OH ₂)	92.8(3) (L = NH ₃)	92.8(3) (L = NO ₂)
O–M(2)–L'	89.4(2) (L' = OH ₂)	92.8(3) (L' = NH ₃)	92.5(3) (L = NO ₂)
M(1)–O– M(2)	165.4(3)	158.2(4)	157.2(3)
L–M(1)– M(2)–L' ^b	65.7 (H ₂ O···OH ₂)	28.5 (H ₃ N···NH ₃)	115.9 (O ₂ N···NO ₂)

^aDistance of separation between adjacent *cis* ligands across the μ -oxo bridge. ^bTorsional angle of L and L' along the M(1)–M(2) axis between the planes containing L–M(1)–O and O–M(2)–L'.

O–Ru units of related structures [(bpy)₂(H₃N)Ru^{III}ORu^{III}(NH₃)(bpy)₂](ClO₄)₄·2H₂O; and [(bpy)₂(O₂N)Ru^{III}ORu^{III}(NO₂)(bpy)₂](ClO₄)₂·2H₂O.

From the data in Table 6, Ru–O distances to the μ -oxo bridge in [(H₂O)Ru^{III}ORu^{III}(OH₂)⁴⁺ (1.869 Å) suggest considerable multiple-bond character. The basis for π bonding along the intersecting Ru–O–Ru bonding axes, as visualized, for example, in Figure 8, arises from $d\pi$ – $p\pi$ – $d\pi$ interaction between the p orbitals of the bridging O and $d\pi$ orbitals at the metal ions.

Terminal Ru–O bond lengths to the aqua ligands (2.136 Å) in the blue dimer are more consistent with Ru^{II}OH₂ complexes [2.1053(16)–2.188(6) Å] than Ru^{III}OH₂ [2.007(3)–] of Ru^{II} rather than Ru^{III} because of cross-bridge $d\pi$ – $p\pi$ – $d\pi$ interactions.

A comparison of Ru–O–Ru angles among the examples in Table 6 shows that the bis(aqua) complex (blue dimer) has the largest angle (165.4°), while the angles in the bis(ammine) (158.2°) and bis(nitro) (157.2°) cations are smaller. As noted elsewhere⁸ and shown in Figure 6, bending along the Ru–O–Ru axis leads to electronic stabilization by removal of the degeneracy of the two half-filled antibonding $d\pi^*$ orbitals

through a Jahn–Teller stabilization to give a doubly occupied, lower-energy state.

The effects of ligand–ligand repulsion can be seen in the magnitude of the dihedral angle between the planes containing L–M(1)–O and O–M(2)–L'. Even though the Ru–O–Ru bond angle for the bis(ammine) complex is only 1° larger than that for the bis(nitro) complex, its H₃N–Ru–Ru–NH₃ dihedral angle is significantly smaller at 28.5° compared to 115.9°. The dihedral angle for the bis(aqua) complex is intermediate between the other two at 65.7°.

Magnetism. The blue dimer is essentially diamagnetic at 2 K, consistent with a singlet ground state. This result is in agreement with reported low-temperature electron paramagnetic resonance (EPR) measurements and the absence of a measurable EPR resonance at 4–5 K.⁴⁰ The magnetic properties are temperature-dependent, with the paramagnetism increasing as the temperature increases. However, the net number of unpaired electrons per dimer is still only ~1.5 for the highest μ_{eff} value at 350 K. The observed paramagnetism at temperatures up to 350 K, therefore, arises from the incomplete thermal population of a low-lying triplet state because two unpaired electrons would be expected for noninteracting or weakly coupled low-spin Ru^{III} $d\pi^5$ ions.

The magnetic susceptibility data for the blue dimer are unusual in that a prominent maximum is not found in the χ – T plot of Figure 1. In antiferromagnetically coupled dimeric systems, such maxima are typically used to obtain the exchange coupling parameter J ($2J$ is the energy splitting between a singlet ground state and a low-lying triplet magnetic excited state). Not surprisingly, attempted fits of the magnetic data by use of the Bleaney–Bowers expression^{41,42} for two interacting sites (each with a one-electron local spin; i.e., $S_a = S_b = 1/2$, $\mathbf{H} = -2J\cdot\mathbf{S}_a\cdot\mathbf{S}_b$) were unable to simulate the temperature-dependent data.

In a previous study, the magnetic behavior of the nitro analogue [(bpy)₂(O₂N)Ru^{III}ORu^{III}(NO₂)(bpy)₂](PF₆)₂ exhibited a more typical temperature dependence from 77 to 275 K, with a maximum appearing in the χ – T plot at ~155 K. In this case, fitting of the data to the Bleaney–Bowers equation gave $2J = -173 \text{ cm}^{-1}$ (with $g = 2.48$).⁷ Possible interpretations of the data were a moderate antiferromagnetic interaction between sites or a strong electronic coupling. The latter was favored based on ancillary evidence based on structural, electronic, and chemical properties.

The room-temperature magnetic moment of the nitro derivative is 1.8 μ_B per Ru^{III}, the expected value for one unpaired electron. The difference in magnetic behavior between the blue dimer and this derivative is likely due to differences in the structural and electronic properties and how they influence electronic coupling. The XRD-determined Ru–O–Ru angle is 157.2° for the *dicationic* nitro analogue and 165.4° for the *tetracationic* blue dimer.

Magnetism in the blue dimer is consistent with other overall experimental/theoretical results obtained and provides additional support for the proposed model, which assumes strong $d\pi$ – $p\pi$ – $d\pi$ interactions and extensive electronic delocalization between Ru^{III} sites (as depicted in Figure 6). In this interpretation, the diamagnetic singlet ground state is delocalized with electronic configuration [$d\pi_1^*$]². The temperature-dependent paramagnetism arises from a thermally populated triplet state of configuration [$d\pi_1^*$]¹[$d\pi_2^*$]¹.

UV–Visible–Near-IR Spectra. The appearance of MLCT transitions in the visible region of the spectrum is a common feature for ruthenium(II) polypyridyl complexes,^{43–46} but these

bands typically appear in the UV for Ru^{III}.³⁹ For example, the MLCT λ_{max} for the most intense low-energy feature for Ru(bpy)₃²⁺ appears at $\lambda_{\text{max}} \sim 460$ nm, while the MLCT λ_{max} for Ru(bpy)₃³⁺ is masked by intense, bpy-based $\pi \rightarrow \pi^*$ transitions between 200 and 300 nm.²⁰

As a consequence, the appearance of MLCT bands at relatively low energy, ~ 580 nm, in the blue dimer is a significant observation, an important consequence of the influence of extensive $d\pi$ - $p\pi$ - $d\pi$ orbital mixing with extensive donation from the bridging oxo group to $d\pi$. The energies of MLCT transitions are directly related to the electron content at the metal, with transition energies significantly increased for Ru^{III} because of electrostatic stabilization of the $d\pi^5$ core. The cross-bridge $d\pi$ - $p\pi$ - $d\pi$ interaction increases the energy of the nonbonding, largely $d\pi$ levels that are the origin of the low-energy MLCT transitions, shifting them from the UV into the visible.^{47,48}

There is a significant difference in solvent dependence for the overlapping MLCT and RuORu bridge-centered transitions. For the MLCT transitions, with a significant difference in dipole character between ground and excited states, absorption band energies are highly solvent-dependent.^{49–55} A far smaller solvent dependence is predicted for the bridge-based $d\pi \rightarrow d\pi^*$ transition given its centrosymmetric origin. A residual solvent dependence is predicted, arising from the bent Ru–O–Ru bridge and the resulting asymmetric change in electronic distribution between ground and excited states.

Low-energy bands of low absorptivity appear in the near-IR for both the Ru^{III}ORu^{III} and Ru^{IV}ORu^{III} forms of the blue dimer (Table 1), arising from $d\pi_{xy} \rightarrow d\pi_2^*$ IC transitions. In related Ru^{III} d^5 monomers, these absorptions appear with low absorptivities and transition energies appearing in the IR, typically below 3000 cm⁻¹.²⁰ The allowedness of these transitions is due to low symmetry and spin-orbit coupling, which induce mixing of the $d\pi$ orbitals. The significant increase in energy and absorptivity for the $d\pi_n \rightarrow d\pi_{xy}$ absorption bands in the dimers is an additional consequence of extensive Ru–O–Ru mixing across the μ -oxo bridge. The “IC” transitions in this case arise from transitions from largely localized d_{xy} orbitals to $d\pi_2^*$.

RR Excitation Profiles. Analysis of the excitation-dependent RR profiles provides additional insight into the electronic origin of the visible absorption bands, with conclusions consistent with the DFT results.

637 nm Band. On the basis of the DFT assignments in Table 5, the absorption at 637 nm arises from overlapping, bridge-based $d\pi_{2n} \rightarrow d\pi_2^*$ and $d\pi_1^* \rightarrow \pi^*(\text{bpy}_1)$ MLCT transitions, with the intensity dominated by the former. Calculated oscillator strengths for the two are 0.34 and 0.059, respectively. (Additional oscillator strengths are included in the SI.)

This assignment is consistent with the observed resonance enhancements of both $\nu_{\text{sym}}(\text{Ru–O–Ru})$ and $\nu(\text{bpy})$ -based modes (Table 3). As shown by the large intensity enhancement for $\nu_{\text{sym}}(\text{Ru–O–Ru})$, there is a significant change in polarization between ground and excited states, with strong coupling and a large displacement change for this mode. A large displacement is qualitatively predicted based on the nature of the transition and excitation of an electron into $d\pi_2^*$, which is antibonding with regard to the Ru–O–Ru interaction. Given its oscillator strength, this transition is strongly dipole-allowed in contrast to $d\pi_{2n} \rightarrow d\pi_2^*$. The change in the electronic

distribution for the transition can be seen in the MOs illustrated in Figure 8.

As noted above, the bent nature of the Ru–O–Ru bridge results in an asymmetrical change in the electronic distribution in the $d\pi_{2n} \rightarrow d\pi_1^*$ transition. Consistent with this conclusion and a contribution from the overlapping MLCT component, there is a solvent dependence for this band in *cis,cis*-[(bpy)₂(Cl)Ru^{III}ORu^{III}(Cl)(bpy)₂]²⁺, as noted in a previous section.

580 nm Band. From the assignments in Table 5, the band at 580 nm is dominated by a second set of $d\pi_{2n} \rightarrow d\pi_1^*$ ($d\pi \rightarrow d\pi^*$) and MLCT transitions, one of which, $d\pi_1^* \rightarrow \pi_2^*(\text{bpy}_1)$, occurs at the same energy. The other two arise from the MLCT transitions $d\pi_1^* \rightarrow \pi_1^*(\text{bpy}_1)$ and $d\pi_1^* \rightarrow \pi_1^*(\text{bpy}_2)$. There is a lesser contribution from a $\pi_2(\text{bpy}_2) \rightarrow d\pi_2^*$ ligand-to-metal charge-transfer (LMCT) transition. The combined $d\pi \rightarrow d\pi^*$ charge-transfer origin for these transitions is consistent with the observed pattern of resonance enhancements for $\nu_{\text{sym}}(\text{Ru–O–Ru})$ and $\nu(\text{bpy})$.

The appearance of overlapping MLCT and LMCT bands and their underlying transitions is a novel feature arising from the μ -oxo bridge and the impact on the $d\pi$ orbitals of strong Ru–O–Ru electronic coupling.

Electrochemical measurements show that $E_{1/2} = 0.66$ V vs NHE for the one-electron reduction of *cis,cis*-[(bpy)₂(H₂O)-Ru^{III}ORu^{III}(OH₂)(bpy)₂]⁴⁺ to *cis,cis*-[(bpy)₂(H₂O)Ru^{III}-ORu^{II}(OH₂)(bpy)₂]³⁺, with the added electron entering $d\pi_2^*$ (Figure 6). The relatively low potential for reduction is consistent with the appearance of LMCT bands at relatively low energies in the visible.

480 nm Band. From Table 5, the intensity of this band is dominated by overlapping $\pi(\text{bpy}) \rightarrow d\pi^*$ LMCT transitions, $\pi_1(\text{bpy}_1) \rightarrow d\pi_2^*$, $\pi_2(\text{bpy}_1) \rightarrow d\pi_2^*$. This assignment is consistent with the observed resonance enhancement of medium-frequency $\nu(\text{bpy})$ modes.

410 and 375 nm Bands. On the basis of the assignments in Table 5, the bands at 410 nm, at 400 nm in [(bpy)₂(Cl)-Ru^{III}ORu^{III}(Cl)(bpy)₂]²⁺, and at 375 nm can similarly be assigned to a series of overlapping $d\pi \rightarrow \pi^*(\text{bpy})$ MLCT bands.

DFT-Optimized Geometries. Previous reports by Baik et al. concluded that the ground state for the blue dimer is a weakly antiferromagnetically coupled singlet, based on DFT calculations.¹² This conclusion was based on a comparison between the calculated and experimental redox potentials. Notably, values calculated based on an antiferromagnetic singlet state were in better agreement with experimental values than values calculated based on a triplet state even though the DFT calculations predict a triplet ground state. In the complete active space multiconfiguration SCF (MC-SCF) calculations of Martin et al., a singlet ground state was calculated as ~ 1000 cm⁻¹ below the triplet.¹¹ The $d\pi$ orbitals were used as the active space, with 10 electrons distributed within the orbital set.

In the Baik calculations, a PCM was used to model the solvent (water) in the calculation of the solvation energies without explicitly considering specific solvent interactions. For *cis,cis*-[(bpy)₂(H₂O)Ru^{III}ORu^{III}(OH₂)(bpy)₂]⁴⁺ and its oxidized forms, strong hydrogen-bonding interactions of the aqua and hydroxo ligands with protic solvents (such as water) are expected and were included in our calculations.

Table 7 lists key geometric features calculated by using different DFT models and compares the results with the actual features from the X-ray structure. (See the SI for details.) Both

Table 7. Comparison between the Experimental and Calculated Structural Features for *cis,cis*-[(bpy)₂(H₂O)Ru^{III}ORu^{III}(H₂O)(bpy)₂]⁴⁺

method	specifics ^a	<i>d</i> (Ru–μ–O), Å	∠(Ru–O–Ru), deg	<i>d</i> (Ru–OH ₂), Å
Martin et al. ¹¹ (CASSCF)	gas phase, weakly, AF-coupled singlet, π symmetry	1.950	173.5	2.235
Baik et al. ¹² (DFT, broken symmetry)	dielectric continuum weakly, AF-coupled singlet, δ symmetry	1.942	172.5	2.255
Bartolotti et al. ¹⁶ (DFT)	gas phase, strongly coupled singlet	1.874	151.6	2.164
this work (DFT)	microsolvation/DC, counterions, strongly coupled singlet	1.905	162.3	2.112
X-ray ²	solid state	1.869	165.4	2.137

^aAbbreviations: AF = antiferromagnetically; DC = dielectric continuum.

Table 8. Structural, Magnetic, and Spectroscopic Data for Ru–O–Ru Complexes

no.	complex	Ru–O–Ru angle (deg)	Mag ^a	Ru–O (Å) ^b	$\bar{\nu}_{\text{sym}}(\text{Ru}^{\text{III}}\text{–O–Ru}^{\text{III}})$	$\bar{\nu}_{\text{asym}}(\text{Ru}^{\text{III}}\text{–O–Ru}^{\text{III}})$	$\bar{\nu}_{\text{max}}^c$ (cm ⁻¹)	ϵ^c (M ⁻¹ cm ⁻¹)
1	[(tpy)(C ₂ O ₄)Ru–O–Ru(C ₂ O ₄)(tpy)] ⁶²	148.5	D	1.843	467	780	15 700	10 500
2	[(tpm)Ru] ₂ O(O ₂ P(O)(OH)) ⁶³	124.6	D	1.870			17 400	16 200
3	[(bpy) ₂ (NO ₂)Ru–O–Ru(NO ₂)(bpy) ₂] ²⁺⁷	157.2	P	1.883			15 800	25 700
4	[(tmtcan) ^d (acac) ^e Ru–O–Ru(acac)(tmtcan)] ²⁺⁶⁴	180	P	1.913	333		16 800	12 400
5	[[py] ₆ Ru] ₂ (O)(CH ₃ CO ₂) ₂] ²⁺⁶⁵	122.2		1.857	597		17 000	10 000
6	[[tmtcan] ₂ Ru] ₂ (O)(CH ₃ CO ₂) ₂] ²⁺⁶⁶	119.7	D	1.884			18 400	6 100
7	[[1-MeIm] ₃ Ru] ₂ (O)(CH ₃ CO ₂) ₂] ²⁺⁶⁷	122.3					20 000	3 600
8	[(bpy) ₂ (NH ₃)Ru–O–Ru(OH)(bpy) ₂] ³⁺¹⁵	153.8		1.878	384	766		
9	[(bpy) ₂ (H ₂ O)Ru–O–Ru(H ₂ O)(bpy) ₂] ⁴⁺²	165.4	P	1.869	382	810	15 700	25 000
10	[(bpy) ₂ (NH ₃)Ru–O–Ru(H ₂ O)(bpy) ₂] ⁴⁺¹⁵	155.9		1.890	378	765		
11	[(bpy) ₂ (NH ₃)Ru–O–Ru(NH ₃)(bpy) ₂] ^{4+8;15}	158.2	P	1.894	384	767	15 800	37 300

^aRoom-temperature magnetism: paramagnetic (P) or diamagnetic (D). ^bRu–μ–oxo bond length. ^c $\bar{\nu}_{\text{max}}$ in cm⁻¹ and molar extinction coefficient in M⁻¹ cm⁻¹ for the intense absorption band in the visible. ^dtmtcan = 1,4,7-trimethyl-1,4,7-triazacyclononane. ^eacac = acetylacetonate. ^f1-MeIm = 1-methylimidazole.

weak coupling models significantly overestimate the Ru–O bridge distance and Ru–O–Ru angle as expected for weak electronic coupling. As shown in the table, features calculated by assuming strong coupling are in better agreement with the XRD results.²

The orbital energy diagram in Figure 6, derived from the current DFT calculations, is qualitatively consistent with changes that occur upon oxidation or reduction and with the electronic absorption spectrum of *cis,cis*-[(bpy)₂(H₂O)Ru^{III}ORu^{III}(OH₂)(bpy)₂]⁴⁺. In an acidic aqueous solution, net 2e⁻ reduction occurs at antibonding level $d\pi_2^*$, resulting in loss of the Ru–O–Ru bridge, [(bpy)₂(H₂O)Ru^{III}ORu^{III}(OH₂)(bpy)₂]⁴⁺ + H₂O $\xrightarrow{+2e^-/2H^+}$ 2 [Ru^{II}(bpy)₂(OH₂)₂]²⁺.⁸ Oxidation and proton loss give asymmetrical *cis,cis*-[(bpy)₂(HO)Ru^{IV}ORu^{III}(OH₂)(bpy)₂]⁴⁺, in which the Ru–μ–O bond lengths decrease to 1.823 and 1.847 Å, consistent with the loss of an electron from antibonding $d\pi_1^*$.

The average Ru–μ–O distance is 1.882 Å in the series [(bpy)₂(L)Ru^{III}ORu^{III}(L)(bpy)₂]ⁿ⁺ (L = H₂O, NH₃, or NO₂⁻; n = 2 or 4),^{2,14,15} 1.835 Å in [(phen)(py-ph)(Cl)Ru^{III}ORu^{IV}(py-ph)(phen)]⁺ [phen = 1,10-phenanthroline; py-ph = 2-(2-pyridyl)phenyl],⁵⁶ and 1.836 Å in [(bpy)₂(Cl)Ru^{III}ORu^{IV}(Cl)(bpy)₂]³⁺. In [(Cl)₅Ru^{IV}ORu^{IV}(Cl)₅]⁴⁻,⁵⁷ [(CH₃CN)₂(Cl)₃Ru^{IV}ORu^{IV}(Cl)₃(CH₃CN)₂],⁵⁸ [(OEP)(Cl)Ru^{IV}ORu^{IV}(Cl)(OEP)] (OEP = octaethylporphyrinato),⁵⁹ and [(PPP)(Cl)Ru^{IV}ORu^{IV}(Cl)(PPP)] [PPP = 5,10,15,20-tetrakis-(pentafluorophenyl)porphyrinato],⁶⁰ the average Ru–O bridge distance is 1.793 Å.

From these results, there is an average decrease of Δ(Ru–μ–O) = –0.092 Å between the III,III and IV,IV oxidation states. Structural data are not available for higher oxidation state

forms. From earlier gas-phase calculations on one rotamer of [(bpy)₂(O)Ru^VORu^V(O)(bpy)₂]⁴⁺, *d*(Ru–μ–O) = 1.856 Å and ∠Ru–O–Ru = 177.6°, with *d*(Ru=O) = 1.723 Å for the terminal oxo groups.¹⁶

RR Energies and Structural Trends. Characteristic symmetric and asymmetric stretches appear for the Ru–O–Ru core in Ru^{III}ORu^{III} near 400 and 800 cm⁻¹. In a series of Fe^{III}OFe^{III} dimers, a correlation has been found between the Fe–O–Fe bond angle and $\bar{\nu}_{\text{sym}}(\text{Fe}^{\text{III}}\text{OFe}^{\text{III}})$ band energies.⁶¹ In this series, $\bar{\nu}_{\text{sym}}(\text{Fe}^{\text{III}}\text{OFe}^{\text{III}})$ decreases as the Fe–O–Fe angle increases, with $\bar{\nu}_{\text{sym}}(\text{Fe}^{\text{III}}\text{OFe}^{\text{III}})$ varying from 550 cm⁻¹ at 120° to 380 cm⁻¹ at 180°. On the basis of data from the same series, $\bar{\nu}_{\text{asym}}(\text{Fe}^{\text{III}}\text{OFe}^{\text{III}})$ increases from 750 cm⁻¹ at 120° to 850 cm⁻¹ at 180°. Table 8 summarizes the structural, magnetic, and spectroscopic data for a series of μ-oxoruthenium complexes.

As shown in Figure 10, structure–band energy correlations found in the Fe^{III}OFe^{III} series also exist for the Ru^{III}ORu^{III} dimers in Table 8. In this series, $\bar{\nu}_{\text{sym}}(\text{Ru}^{\text{III}}\text{ORu}^{\text{III}})$ varies from 597 cm⁻¹ at 122° to 333 cm⁻¹ at 180°, while $\bar{\nu}_{\text{asym}}(\text{Ru}^{\text{III}}\text{ORu}^{\text{III}})$ varies from 780 cm⁻¹ at 148° to 810 cm⁻¹ at 165°. An unambiguous linear trend is observed when plotting $\bar{\nu}_{\text{sym}}$ versus ∠Ru–O–Ru (Figure 10a).

Qualitatively, the magnitude of ∠M–O–M and the bending away from linearity and 180° represent a balance between electronic stabilization and ligand-based electron–electron repulsion. The bending can be viewed as a Jahn–Teller distortion, which results in electronic stabilization by the lifting of degeneracy in the doubly occupied $d\pi_1^*$ and $d\pi_2^*$ levels (Figure 6). As the M–O–M angle becomes more acute, ligand–ligand repulsion increases. The final structures are a compromise between the two.

The energy separation between singlet ground, ($d\pi_1^*$)², and triplet excited, ($d\pi_1^*$)¹(π_2^*), states depends on the exchange

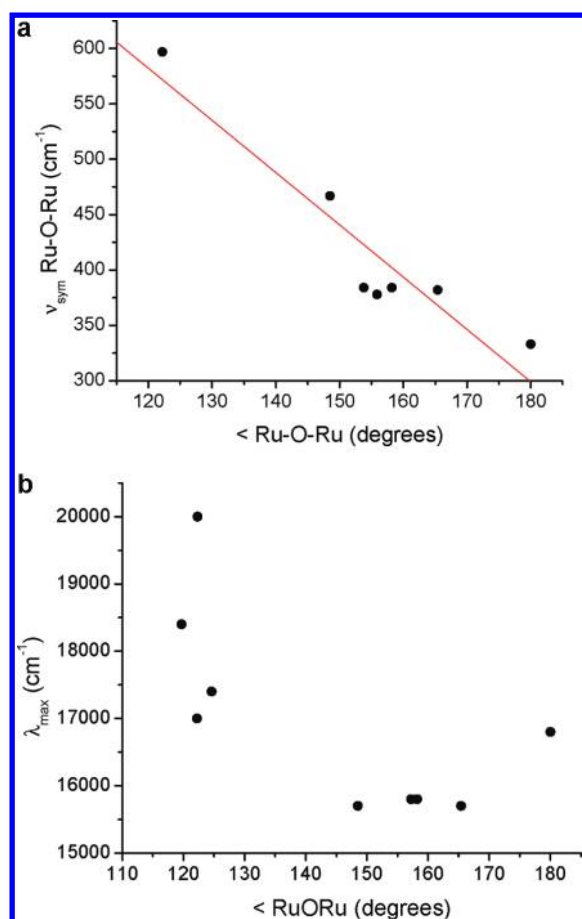


Figure 10. (a) Plot of $\nu_{\text{sym}}(\text{Ru-O-Ru})$ vs $\angle\text{Ru-O-Ru}$ for complexes in Table 8. (b) As in Figure 9a, variation in the energy of the intense, low-energy visible $d\pi_1^* \rightarrow \pi_2^*$ absorption band with $\angle\text{Ru-O-Ru}$.

energy and the energy difference between $d\pi_1^*$ and $d\pi_2^*$. The latter is highly sensitive to $\angle\text{Ru-O-Ru}$, as can be seen in the data in Table 8. Although the data are limited, a cutoff between the diamagnetic and paramagnetic ground states appears to occur at an angle near 150° . Below this angle, the energy separation between $d\pi_1^*$ and $d\pi_2^*$ is sufficient to overcome the pairing energy and the ground state is diamagnetic with the valence configuration $(d\pi_1^*)^2$. Above this angle, the energy separation is decreased and the complexes are paramagnetic, $(d\pi_1^*)^1(d\pi_2^*)^1$.

X-ray Photoelectron Spectroscopy (XPS). Ru $3d_{5/2}$ XPS binding energies have been reported for blue dimer analogues $[(\text{bpy})_2\text{ClRu}^{\text{III}}\text{ORu}^{\text{III}}\text{Cl}(\text{bpy})_2](\text{PF}_6)_2$, $[(\text{bpy})_2(\text{O}_2\text{N})\text{Ru}^{\text{III}}\text{ORu}^{\text{III}}(\text{NO}_2)(\text{bpy})_2](\text{ClO}_4)_2$, and mixed-valence $[(\text{bpy})_2\text{ClRu}^{\text{II}}\text{ORu}^{\text{III}}\text{Cl}(\text{bpy})_2](\text{PF}_6)_3$. Comparisons of the binding energies for the related monomers $\text{Ru}^{\text{II}}(\text{bpy})_2\text{Cl}_2$ and $[\text{Ru}^{\text{III}}(\text{bpy})_2\text{Cl}_2]\text{Cl}$ are revealing. Both $\text{Ru}^{\text{III}}\text{ORu}^{\text{III}}$ dimers have Ru $3d_{5/2}$ binding energies of 280.5 eV, closer to the value expected for Ru^{II} [279.9 eV for $\text{Ru}(\text{bpy})_2\text{Cl}_2$] than Ru^{III} [281.9 eV for $[\text{Ru}(\text{bpy})_2\text{Cl}_2]\text{Cl}$]. In the XPS spectrum of the mixed-valence salt, there is a single Ru $3d_{5/2}$ binding energy of 282.3 eV,⁷ consistent with delocalization, $[\text{ClRu}^{\text{III.5}}\text{ORu}^{\text{III.5}}\text{Cl}]^{3+}$.

Electrochemistry. On the basis of an analysis by Taube and Richardson, the comproportionation constant among three adjacent oxidation states for a mixed-valence system, K_C in Scheme 2, provides a measure of the stabilization of the mixed-valence form. It is determined by the difference in the

Scheme 2. Mixed-Valence Equilibrium



potentials between adjacent $1e^-$ couples, E_1 and E_2 , with $\log(K_C) = 16.9(E_2 - E_1) = 16.9\Delta E$ at 25°C .⁶⁸

Although K_C is a measure of the degree of stabilization in the mixed-valence forms of these couples, it includes the effects of electrostatic interactions, solvation effects, and redox asymmetry as well as electronic delocalization.⁷³ In the absence of any interactions, $K_C = 4$ from statistical effects for a complex with equivalent redox sites. Large values are observed for complexes with strong electronic coupling.^{74–76}

Table 9 lists E and ΔE values for adjacent μ -oxo-bridged IV–IV/IV–III and IV–III/III–III couples and for III–III/III–II

Table 9. Electrochemical Data for adjacent $1e^-$ Redox Couples for Ru–O–Ru-Bridged Complexes and Calculated Comproportionation Constants K_C (Scheme 2) Shown below the Reduction Potentials (i Is Irreversible; References Included after the Compound Name)

compound	reduction potential (V vs NHE)			
	E_1° [IV–IV]/ [III–IV]	E_2° [III–IV]/ [III–III]	E_3° [III–III]/ [II–III]	E_4° [II–III]/ [II–II]
$[(\text{HCO}_2)(\text{NH}_3)_4\text{Ru-O-Ru}(\text{NH}_3)_4(\text{O}_2\text{CH})]^{3+ a, 69}$	1.17	0.00	$\sim 0.40 i$	
				6.0×10^{19}
$[(\text{Cl})(\text{NH}_3)_4\text{Ru-O-Ru}(\text{NH}_3)_4(\text{Cl})]^{3+ a, 69}$	1.03	0.18	$\sim 0.18 i$	
				2.3×10^{14}
$[(\text{NH}_3)_3\text{Ru-O-Ru}(\text{NH}_3)_3]^{3+ b, 69}$	1.91	0.56	-1.74	
				6.6×10^{22}
$[(\text{tpa})\text{ClRu-O-RuCl}(\text{tpa})]^{2+ c, 70}$	1.99	0.75		
				9.2×10^{20}
$[(\text{bpy})_2\text{ClRu-O-RuCl}(\text{bpy})_2]^{2+ c, 7}$	2.15	0.92	-0.08	$-0.76 i$
				6.2×10^{20}
$[(\text{bpy})_2(\text{O}_2\text{N})\text{Ru-O-Ru}(\text{NO}_2)(\text{bpy})_2]^{2+ c, 7}$	$\sim 2.44 i$	1.18	0.09	$\sim -0.51 i$
				2.0×10^{21}
$[(\text{bpy})_2(\text{py})\text{Ru-O-Ru}(\text{NCCH}_3)(\text{bpy})_2]^{4+ d, 71}$		1.51	0.42	$-0.45 i$
				5.1×10^{14}
$[(\text{bpy})_2(\text{py})\text{Ru-O-Ru}(\text{OH}_2)(\text{bpy})_2]^{4+ d, 71}$	1.60	1.18		
				1.3×10^7
$[(\text{bpy})_2(\text{py})\text{Ru-O-Ru}(\text{py})(\text{bpy})_2]^{4+ d, 71}$		1.50	0.45	$-0.47 i$
				3.6×10^{15}
$[(\text{bpy})_2(\text{H}_2\text{O})\text{Ru-O-Ru}(\text{OH}_2)(\text{bpy})_2]^{4+ e, 3}$	> 1.45	1.04	0.30 i	
				$> 10^7$
$[(\text{bpy})_2(\text{HO})\text{Ru-O-Ru}(\text{OH})(\text{bpy})_2]^{2+ f, 72}$	0.67	0.46		
				3.5×10^3

^a0.1 M LiCl, aqueous, various pHs. ^b0.1 M LiClO₄, acetonitrile. ^c0.1 M NBu₄PF₆, acetonitrile. ^d0.1 M NEt₄ClO₄, acetonitrile. ^e0.1 M CF₃SO₃H. ^f1.0 M NaOH.

and III–II/II–II couples where the data are available. The substantial values of K_C for the equilibrium IV–IV + III–III = 2IV–III of up to 6.6×10^{22} are an impressive demonstration of highly stabilized mixed-valence forms of these complexes.

Measurements on the equilibrium $\text{III-III} + \text{II-II} = 2\text{III-II}$ are complicated by the instability of the reduced complexes toward loss of the μ -oxo bridge due to reduction at $d\pi_2^*$, which, as noted above, results in irreversibility. Nonetheless, from the limited data set in Table 9, K_C values of up to 3.6×10^{15} illustrate the importance of electronic coupling for this equilibrium as well. As discussed elsewhere, additional electrochemical and pK_a comparisons reveal the profound influence of cross-bridge electronic coupling in the blue dimer and related complexes.⁶

Water Exchange Rates. The impact of electronic coupling also appears in substitution rates. The rate constant for water exchange in $[(\text{bpy})_2(\text{H}_2\text{O})\text{Ru}^{\text{III}}\text{ORu}^{\text{III}}(\text{OH}_2)(\text{bpy})_2]^{4+}$ at 23 °C is $k = 7 \times 10^{-3} \text{ s}^{-1}$. This is comparable to water exchange in ruthenium(II) aqua complexes with $k = \sim 2 \times 10^{-2} \text{ s}^{-1}$ for $\text{Ru}(\text{OH}_2)_6^{2+}$ with substitution at Ru^{III} far slower with $k \sim 4 \times 10^{-6} \text{ s}^{-1}$ for $\text{Ru}(\text{OH}_2)_6^{3+}$.⁹

CONCLUSIONS

In contrast to conclusions reached earlier based on DFT and CASSCF calculations,^{11,12} the accumulated experimental evidence shows that strong, cross-bridge electronic coupling plays a major role in dictating the electronic and molecular structural properties of $[(\text{bpy})_2(\text{H}_2\text{O})\text{Ru}^{\text{III}}\text{ORu}^{\text{III}}(\text{OH}_2)(\text{bpy})_2]^{4+}$:

- (i) Structural comparisons show that multiple Ru–O bonding exists in the μ -oxo bridge. Ru–OH₂ bond distances are more characteristic of Ru^{II} than Ru^{III}.
- (ii) Comproportionation constants for the equilibria $\text{IV-IV} + \text{III-III} = 2 \text{IV-III}$, with $K_C > 10^{22}$, and $\text{III-III} + \text{II-II} = 2 \text{III-II}$, with $K_C > 10^{15}$, are consistent with strong coupling between sites.
- (iii) Electrochemical reduction results in facile cleavage of the μ -oxo bridge consistent with reduction occurring at delocalized, antibonding $d\pi^*$ orbitals at the μ -oxo bridge.
- (iv) Magnetic measurements are consistent with a delocalized, diamagnetic singlet ground state, with a low-lying triplet explaining the temperature-dependent paramagnetism.
- (v) Electrochemical, pK_a , and water exchange rate comparisons all point to ruthenium sites with the electron content more closely resembling Ru^{II} than Ru^{III}. This conclusion is reinforced by XPS binding energy comparisons.
- (vi) The electronic absorption spectrum can be assigned quantitatively by DFT by assuming a delocalized model and singlet ground state when specific hydrogen-bonding interactions with surrounding solvent water molecules are included. The visible spectrum is dominated by an intense, $d\pi_n \rightarrow d\pi^*$ Ru–O–Ru bridge-based transition overlapped with a $d\pi \rightarrow \pi^*(\text{bpy})$ MLCT transition.
- (vii) A $\text{Ru}^{\text{III}} \rightarrow \text{bpy}$ MLCT transition appears in the visible, while MLCT transitions in related ruthenium(III) complexes appear in the UV.
- (viii) The delocalized electronic structural model is consistent with RR excitation profiles and resonant enhancement of the ν_{sym} and ν_{asym} (Ru–O–Ru) modes upon excitation into Ru–O–Ru-centered transitions.
- (ix) IC absorption bands appear at significantly higher energies compared to related ruthenium(III) monomers because of electronic delocalization and destabilization of the lowest $d\pi$ acceptor orbitals, $d\pi_2^*$.

- (x) Magnetic properties are sensitive to $\angle\text{Ru-O-Ru}$, with bending along this axis removing the degeneracy of the $d\pi^*$ levels and disfavoring the triplet state $(d\pi_1^*)^1(d\pi_2^*)^1$ while stabilizing $(d\pi_1^*)^2$. The equilibrium angle is a compromise between the associated stabilization energy and ligand–ligand repulsion.

ASSOCIATED CONTENT

Supporting Information

Details of DFT calculations (excited states, oscillator strengths, and Cartesian coordinates), comparisons between calculated and experimental absorption spectra, experimental absorption spectra of $[(\text{bpy})_2\text{ClRuORuCl}(\text{bpy})_2](\text{PF}_6)_2$ in various solvents, a plot showing the magnetic field dependence of magnetization for the blue dimer. This material is available free of charge via the Internet at <http://pubs.acs.org>.

AUTHOR INFORMATION

Corresponding Author

*E-mail: tjmeyer@unc.edu.

ACKNOWLEDGMENTS

Funding by the Chemical Sciences, Geosciences and Biosciences Division of the Office of Basic Energy Sciences, U.S. Department of Energy (Grant DE-FG02-06ER15788), and UNC EFRC: Solar Fuels and Next Generation Photovoltaics, an Energy Frontier Research Center funded by the U.S. Department of Energy, Office of Science, Office of Basic Energy Sciences, under Award DE-SC0001011 is gratefully acknowledged. The work at LANL was supported by the U.S. Department of Energy through the Laboratory Directed Research & Development (LDRD) program.

REFERENCES

- (1) Gersten, S. W.; Samuels, G. J.; Meyer, T. J. *J. Am. Chem. Soc.* **1982**, *104*, 4029.
- (2) Gilbert, J. A.; Eggleston, D. S.; Murphy, W. R.; Geselowitz, D. A.; Gersten, S. W.; Hodgson, D. J.; Meyer, T. J. *J. Am. Chem. Soc.* **1985**, *107*, 3855.
- (3) Binstead, R. A.; Chronister, C. W.; Ni, J. F.; Hartshorn, C. M.; Meyer, T. J. *J. Am. Chem. Soc.* **2000**, *122*, 8464.
- (4) Yamada, H.; Siems, W. F.; Koike, T.; Hurst, J. K. *J. Am. Chem. Soc.* **2004**, *126*, 9786.
- (5) Hurst, J. K.; Cape, J. L.; Clark, A. E.; Das, S.; Qin, C. Y. *Inorg. Chem.* **2008**, *47*, 1753.
- (6) Liu, F.; Concepcion, J. J.; Jurss, J. W.; Cardolaccia, T.; Templeton, J. L.; Meyer, T. J. *Inorg. Chem.* **2008**, *47*, 1727.
- (7) Weaver, T. R.; Meyer, T. J.; Adeyemi, S. A.; Brown, G. M.; Eckberg, R. P.; Hatfield, W. E.; Johnson, E. C.; Murray, R. W.; Untereker, D. *J. Am. Chem. Soc.* **1975**, *97*, 3039.
- (8) Schoonover, J. R.; Ni, J. F.; Roecker, L.; White, P. S.; Meyer, T. J. *Inorg. Chem.* **1996**, *35*, 5885.
- (9) Yamada, H.; Koike, T.; Hurst, J. K. *J. Am. Chem. Soc.* **2001**, *123*, 12775.
- (10) (a) Concepcion, J. J.; Jurss, J. W.; Templeton, J. L.; Meyer, T. J. *J. Am. Chem. Soc.* **2008**, *130* (49), 16462. (b) Concepcion, J. J.; Jurss, J. W.; Norris, M. R.; Chen, Z. F.; Templeton, J. L.; Meyer, T. J. *Inorg. Chem.* **2010**, *49*, 1277. (c) Concepcion, J. J.; Tsai, M.-K.; Muckerman, J. T.; Meyer, T. J. *J. Am. Chem. Soc.* **2010**, *132* (5), 1545. (d) Wang, L.-P.; Wu, Q.; Voorhis, T. V. *Inorg. Chem.* **2010**, *49*, 4543.
- (11) Batista, E. R.; Martin, R. L. *J. Am. Chem. Soc.* **2007**, *129*, 7224.
- (12) (a) Yang, X. F.; Baik, M. H. *J. Am. Chem. Soc.* **2004**, *126*, 13222. (b) Yang, X.; Baik, M. H. *J. Am. Chem. Soc.* **2006**, *128*, 7476.
- (13) Bianco, R.; Hay, P. J.; Hynes, J. T. *J. Phys. Chem. A* **2011**, *115*, 8003.

- (14) Phelps, D. W.; Kahn, E. M.; Hodgson, D. J. *Inorg. Chem.* **1975**, *14*, 2486.
- (15) Ishitani, O.; White, P. S.; Meyer, T. J. *Inorg. Chem.* **1996**, *35*, 2167.
- (16) Bartolotti, L. J.; Pedersen, L. G.; Meyer, T. J. *Int. J. Quantum Chem.* **2001**, *83*, 143.
- (17) Myers, A. B. *Acc. Chem. Res.* **1997**, *30*, 519.
- (18) Frisch, M. J.; et al. *Gaussian 03*, revision C.02; Gaussian, Inc.: Wallingford, CT, 2004.
- (19) Dobson, J. C.; Sullivan, B. P.; Doppelt, P.; Meyer, T. J. *Inorg. Chem.* **1988**, *27*, 3863.
- (20) (a) Fleming, C. N.; Dattelbaum, D. M.; Thompson, D. W.; Ershov, A. Y.; Meyer, T. J. *J. Am. Chem. Soc.* **2007**, *129*, 9622. (b) Demadis, K. D.; Dattelbaum, D. M.; Kober, E. M.; Concepcion, J. J.; Paul, J. J.; Meyer, T. J.; White, P. S. *Inorg. Chim. Acta* **2007**, *360*, 1143.
- (21) Heller, E. J. *Acc. Chem. Res.* **1981**, *14*, 368.
- (22) Myers, A. B.; Mathies, R. A. *Biological Applications of Raman Spectroscopy*; Wiley and Sons: New York, 1988.
- (23) Myers, A. B.; Mathies, R. A.; Tannor, D. J.; Heller, E. J. *J. Chem. Phys.* **1982**, *77*, 3857.
- (24) Li, B. L.; Myers, A. B. *J. Phys. Chem.* **1990**, *94*, 4051.
- (25) Thompson, D. G.; Schoonover, J. R.; Timpson, C. J.; Meyer, T. J. *J. Phys. Chem. A* **2003**, *107*, 10250.
- (26) Mallick, P. K.; Danzer, G. D.; Strommen, D. P.; Kincaid, J. R. *J. Phys. Chem.* **1988**, *92*, 5628.
- (27) Strommen, D. P.; Mallick, P. K.; Danzer, G. D.; Lumpkin, R. S.; Kincaid, J. R. *J. Phys. Chem.* **1990**, *94*, 1357.
- (28) Omberg, K. M.; Schoonover, J. R.; Treadway, J. A.; Leasure, R. M.; Dyer, R. B.; Meyer, T. J. *J. Am. Chem. Soc.* **1997**, *119*, 7013.
- (29) Dunitz, J. D.; Orgel, L. E. *J. Chem. Soc.* **1953**, 2594.
- (30) Tatsumi, K.; Hoffmann, R. *J. Am. Chem. Soc.* **1981**, *103*, 3328.
- (31) Fodor, L.; Lendvay, G.; Horvath, A. *J. Phys. Chem. A* **2007**, *111*, 12891.
- (32) Lu, Z. A.; Zhang, Q. L.; Xu, Y. S.; Wang, M. L.; Liu, J. H. *J. Theor. Comput. Chem.* **2009**, *8*, 631.
- (33) Charlot, M. F.; Aukauloo, A. *J. Phys. Chem. A* **2007**, *111*, 11661.
- (34) Baik, M. H.; Friesner, R. A. *J. Phys. Chem. A* **2002**, *106*, 7407.
- (35) Bernhard, P.; Burgi, H. B.; Hauser, J.; Lehmann, H.; Ludi, A. *Inorg. Chem.* **1982**, *21*, 3936.
- (36) Sauaia, M. G.; Tfouni, E.; Santos, R. H. D.; Gambardella, M. T. D.; Del Lama, M.; Guimaraes, L. F.; da Silva, R. S. *Inorg. Chem. Commun.* **2003**, *6*, 864.
- (37) Qvortrup, K.; McKenzie, C. J.; Bond, A. D. *Acta Crystallogr., Sect. E: Struct. Rep. Online* **2007**, *63*, M1400.
- (38) Jude, H.; White, P. S.; Dattelbaum, D. M.; Rocha, R. C. *Acta Crystallogr., Sect. E: Struct. Rep. Online* **2008**, *64*, M1388.
- (39) Durham, B.; Wilson, S. R.; Hodgson, D. J.; Meyer, T. J. *J. Am. Chem. Soc.* **1980**, *102*, 600.
- (40) Lei, Y. B.; Hurst, J. K. *Inorg. Chem.* **1994**, *33*, 4460.
- (41) Kahn, O. *Molecular Magnetism*; VCH: New York, 1993.
- (42) Bleaney, B.; Bowers, K. D. *Proc. R. Soc. London, Ser. A* **1952**, *214*, 451.
- (43) Anderson, P. A.; Deacon, G. B.; Haarmann, K. H.; Keene, F. R.; Meyer, T. J.; Reitsma, D. A.; Skelton, B. W.; Strouse, G. F.; Thomas, N. C.; Treadway, J. A.; White, A. H. *Inorg. Chem.* **1995**, *34*, 6145.
- (44) Zhang, G.; Zong, R.; Tseng, H. W.; Thummel, R. P. *Inorg. Chem.* **2008**, *47*, 990.
- (45) Sens, C.; Rodriguez, M.; Romero, I.; Llobet, A.; Parella, T.; Benet-Buchholz, J. *Inorg. Chem.* **2003**, *42*, 8385.
- (46) Ross, H. B.; Boldaji, M.; Rillema, D. P.; Blanton, C. B.; White, R. P. *Inorg. Chem.* **1989**, *28*, 1013.
- (47) Hudson, A.; Kennedy, M. J. *J. Chem. Soc. A* **1969**, 1116.
- (48) Bhattacharya, S.; Ghosh, P.; Chakravorty, A. *Inorg. Chem.* **1985**, *24*, 3224.
- (49) Chen, P. Y.; Meyer, T. J. *Chem. Rev.* **1998**, *98*, 1439.
- (50) Neyhart, G. A.; Timpson, C. J.; Bates, W. D.; Meyer, T. J. *J. Am. Chem. Soc.* **1996**, *118*, 3730.
- (51) North, A. M.; Pethrick, R. A.; Kryszewski, M.; Nadolski, B. *Acta Phys. Pol., A* **1978**, *54*, 797.
- (52) Nadolski, B.; Uznanski, P.; Kryszewski, M. *J. Macromol. Sci., Part B: Phys.* **1984**, *B23*, 221.
- (53) Moya, M. L.; Rodriguez, A.; Sanchez, F. *Inorg. Chim. Acta* **1992**, *197*, 227.
- (54) Dodsworth, E. S.; Lever, A. B. P. *Inorg. Chem.* **1990**, *29*, 499.
- (55) Dodsworth, E. S.; Lever, A. B. P. *Coord. Chem. Rev.* **1990**, *97*, 271.
- (56) Ryabov, A. D.; Le Lagadec, R.; Estevez, H.; Toscano, R. A.; Hernandez, S.; Alexandrova, L.; Kurova, V. S.; Fischer, A.; Sirlin, C.; Pfeffer, M. *Inorg. Chem.* **2005**, *44*, 1626.
- (57) Efimenko, I. A.; Balakaeva, T. A.; Kurbakova, A. P.; Gorbunova, Y. E.; Mikhailov, Y. N. *Koord. Khim.* **1994**, *20*, 294.
- (58) Tyrlik, S. K.; Kisielinska, M.; Huffman, J. C. *Transition Met. Chem.* **1995**, *20*, 413.
- (59) Masuda, H.; Taga, T.; Osaki, K.; Sugimoto, H.; Mori, M.; Ogoshi, H. *Bull. Chem. Soc. Jpn.* **1982**, *55*, 3887.
- (60) Zhang, J. L.; Che, C. M. *Chem.—Eur. J.* **2005**, *11*, 3899.
- (61) Mukherjee, R. N.; Stack, T. D. P.; Holm, R. H. *J. Am. Chem. Soc.* **1988**, *110*, 1850.
- (62) Lebeau, E. L.; Adeyemi, S. A.; Meyer, T. J. *Inorg. Chem.* **1998**, *37*, 6476.
- (63) Llobet, A.; Curry, M. E.; Evans, H. T.; Meyer, T. J. *Inorg. Chem.* **1989**, *28*, 3131.
- (64) Sudha, C.; Mandal, S. K.; Chakravarty, A. R. *Inorg. Chem.* **1993**, *32*, 3801.
- (65) Cipriano, C.; Clark, R. J. H.; Oprescu, D.; Withnall, R. J. *Chem. Soc., Dalton Trans.* **1995**, 2417.
- (66) Neubold, P.; Wiegardt, K.; Nuber, B.; Weiss, J. *Inorg. Chem.* **1989**, *28*, 459.
- (67) Schneider, R.; Weyhermuller, T.; Wiegardt, K.; Nuber, B. *Inorg. Chem.* **1993**, *32*, 4925.
- (68) Richardson, D. E.; Taube, H. *Coord. Chem. Rev.* **1984**, *60*, 107.
- (69) Emerson, J.; Clarke, M. J.; Ying, W. L.; Sanadi, D. R. *J. Am. Chem. Soc.* **1993**, *115*, 11799.
- (70) Koshi, C.; Umakoshi, K.; Sasaki, Y. *Chem. Lett.* **1997**, 1155.
- (71) Doppelt, P.; Meyer, T. J. *Inorg. Chem.* **1987**, *26*, 2027.
- (72) Kutner, W.; Gilbert, J. A.; Tomaszewski, A.; Meyer, T. J.; Murray, R. W. *J. Electroanal. Chem.* **1986**, *205*, 185.
- (73) Browne, W. R.; Hage, R.; Vos, J. G. *Coord. Chem. Rev.* **2006**, *250*, 1653.
- (74) Neyhart, G. A.; Hupp, J. T.; Curtis, J. C.; Timpson, C. J.; Meyer, T. J. *J. Am. Chem. Soc.* **1996**, *118*, 3724.
- (75) Barriere, F.; Camire, N.; Geiger, W. E.; Mueller-Westerhoff, U. T.; Sanders, R. *J. Am. Chem. Soc.* **2002**, *124*, 7262.
- (76) D'Alessandro, D. M.; Keene, F. R. *Dalton Trans.* **2004**, 3950.